Environmental Research 299 (2026) 124321

Contents lists available at ScienceDirect

Environmental Research

journal homepage: www.elsevier.com/locate/envres

Black diamond and black silicon for reducing marine biofilm formation

M.J. Romeu [a], L.C. Gomes [a], R. Teixeira-Santos [a], G. Zulpukarova [b], W. Woudstra [c], J. Atema-Smit [c], G. Geertsema-Doornbusch [c], R. Schirhagl [c,*], P.W. May [b], F.J. Mergulhão [a,**]

[a] *LEPABE – Laboratory for Process Engineering, Environment, Biotechnology and Energy, ALiCE – Associate Laboratory in Chemical Engineering, Faculty of Engineering, University of Porto, Rua Dr. Roberto Frias, 4200-465, Porto, Portugal*

[b] *School of Chemistry, University of Bristol, Bristol, BS8 1TS, United Kingdom*

[c] *Groningen University, University Medical Center Groningen, Antonius Deusinglaan 1, 9713 AV, Groningen, the Netherlands*

ARTICLE INFO

Keywords:
Marine biofilms
Antifouling surfaces
Nanostructured surfaces
Diamond coatings

ABSTRACT

Marine biofilms quickly colonize submerged surfaces, causing drag, reduced efficiency, and corrosion in vessels and marine infrastructure. Thus, the development of coatings that can resist bacterial adhesion and biofilm growth is essential. This study investigated two nanostructured surfaces - black silicon (bSi) and diamond-coated black silicon (black diamond, bD) - designed to physically disrupt bacterial cells using nanoscale spikes. Hydrogen- and fluorine-terminated versions of these surfaces were evaluated against 7-week-old *Cobetia marina* biofilms under controlled hydrodynamic conditions using flat silicon (Flat-Si) and flat diamond as controls. Nanostructured surfaces were less wettable than Flat-Si, with the contact angle of the fluorinated black diamond (bD-F) reaching 132°. Scanning Electron Microscopy confirmed that bSi and bD maintained their high-aspect-ratio nanoneedles, resisted protein adsorption, and had reduced biofilm coverage compared to flat controls. Optical Coherence Tomography revealed ~50% thinner and less porous biofilms on the bD-F surface. Confocal Laser Scanning Microscopy analysis showed a 75% reduction in biofilm biovolume on bD-F compared to Flat-Si, with only 45% cell viability. Non-viable cells were predominantly located in inner biofilm layers, indicating a bactericidal effect. Flow cytometry supported these results, showing altered bacterial membrane potential and metabolic activity in bacteria exposed to bD surfaces. Experiments using real seawater and field immersion assays confirmed that bD surfaces maintain structural integrity and strongly reduce biofilm formation under realistic marine conditions. These findings demonstrate the antifouling and antimicrobial effects of nanostructured diamond-coated surfaces, particularly fluorine-terminated ones, for durable marine applications.

1. Introduction

When immersed in seawater, surfaces gradually become covered by organic matter and, typically, within less than a day, microbial colonization occurs (Flemming and Wingender, 2010). As bacteria grow, they clump together to form biofilms that are difficult to remove and have several detrimental effects. On the hulls of ships, biofilms can increase fuel consumption, reduce speed, and increase maintenance costs. On marine structures, such as bridges or oil rigs, biofilms can obstruct water flow rates, reduce heat-transfer efficiency, and cause microbiologically influenced corrosion. Bacteria can also form multispecies biofilms with other microorganisms, such as microalgae. These can cause microfouling and encourage the adhesion of larger organisms such as algae, mussels and barnacles, which cause macrofouling, blocking water pipes, inlets and outlets (Carvalho, 2018). Unsurprisingly, these problems cause trillions of US dollars in economic losses annually to industries, including marine transport, aquaculture, oil and gas, and desalination (Qian et al., 2022). Furthermore, biofouling contributes to the spread of exotic species transported on vessel hulls across geographic regions, compromising marine ecosystems (Lacoursière-Roussel et al., 2016).

---

* Corresponding author.

** Corresponding author. LEPABE - Laboratory for Process Engineering, Environment, Biotechnology and Energy, Faculty of Engineering, University of Porto, Rua Dr. Roberto Frias, 4200-465, Porto, Portugal.

E-mail addresses: mariaromeu@fe.up.pt (M.J. Romeu), luciana.gomes@fe.up.pt (L.C. Gomes), ritadtsantos@fe.up.pt (R. Teixeira-Santos), iv21161@bristol.ac.uk (G. Zulpukarova), w.woudstra@umcg.nl (W. Woudstra), j.atema-smit@umcg.nl (J. Atema-Smit), g.i.geertsema-doornbusch@umcg.nl (G. Geertsema-Doornbusch), romana.schirhagl@gmail.com (R. Schirhagl), Paul.May@bristol.ac.uk (P.W. May), filipem@fe.up.pt (F.J. Mergulhão).

https://doi.org/10.1016/j.envres.2026.124321
Received 17 July 2025; Received in revised form 29 December 2025; Accepted 18 March 2026

To address this issue, many different materials and coatings have been developed to reduce biofilm formation. These include antimicrobial peptide coatings (Doiron et al., 2018; Herzberg et al., 2021), paints with antimicrobial additives (Neves et al., 2022; Tang and Cooney, 1998), coatings which cause the formation of reactive oxygen species (Park et al., 2020), materials with a high density of positive charges (López Cascales et al., 2018; Yang et al., 2018), or enzymatic materials which degrade substances essential for biofilm formation (Karyani et al., 2023). Also, hydrophobic coatings or surface functionalization have been shown to reduce marine biofilm formation (Carvalho et al., 2025; Xie et al., 2021). Alternatively, eco-friendly strategies employing antimicrobial and antifouling compounds derived from marine organisms (e.g., squid, shrimp, algae or plants) have been developed. Marine coatings based on chitosan, alone (Lima et al., 2022) or in combination with squid-derived melanin (Ghattavi et al., 2023) or plant-derived zinc oxide (ZnO) (Ghattavi et al., 2024) nanoparticles (NPs), demonstrated promising antifouling performance in laboratory or field immersion tests. Similarly, biohybrid NPs of copper oxide-melanin (Ghattavi et al., 2025) or ZnO-silicon oxide (Ghattavi and Homaei, 2024) produced coatings with enhanced antifouling performance. Despite all these developments, marine biofilm formation continues to be a problem.

An interesting alternative for achieving an antimicrobial effect is to use surfaces with a nanoscale structure that repels or kills bacteria upon contact (Ding et al., 2018; Jenkins et al., 2021; Luan et al., 2018; Paxton et al., 2021; Ziębowicz et al., 2021). Black silicon, which is silicon with sharp nanoscale needle structures etched into the surface, is a promising candidate to reduce marine biofilm formation. The material, which owes its name to its black colour resulting from its multiwavelength light absorption, has shown promising results in reducing medical biofilms. This has been demonstrated by Linklater et al. (2017), who have shown that black silicon can reduce the attachment of *Pseudomonas aeruginosa* and *Staphylococcus aureus*. Bhadra et al. (2018) investigated the effect of similar needle geometries on bactericidal efficiency. They found that the sharp needles can penetrate the bacterial membrane, rupturing it and killing the bacterium. Ivanova et al. (2013) compared the bactericidal activity of black silicon with the bactericidal activity of dragonfly wings, which exhibit similar nanostructures on their surface. Alongside the bactericidal activity toward bacteria such as *P. aeruginosa*, *S. aureus* and *Bacillus subtilis*, they found that even *B. subtilis* spores were pierced and killed by black silicon.

The advantage of killing bacteria via a mechanical method like this, rather than chemically, is that it is much harder for bacteria to develop resistance to mechanically fatal mechanisms, as this would generally require them evolving a significant restructuring of the bacteria's size, membrane, and/or morphology, which might require multiple separate mutations to work synchronously. Therefore, it is no surprise that nature uses mechanical bactericidal methods to protect the wings of insects such as cicadas and dragonflies, and that these methods have remained successful for millions of years.

However, one of the main drawbacks of black silicon for antimicrobial surfaces is the poor mechanical stability of the brittle silicon needles (Hazell et al., 2018), which are rather fragile and can be damaged simply by touching them. To solve this issue, black silicon was coated with a thin but conformal layer of diamond using a chemical vapour deposition (CVD) process, to produce 'black diamond'. As a result, the needle structure is retained with a small reduction in sharpness, but the diamond layer renders the needles significantly more robust. While diamond itself is inert and has no antibacterial properties (Norouzi et al., 2020, 2022; Ong et al., 2018), we have shown that black diamond needles can still pierce and/or rupture bacterial cell walls and thus kill and/or reduce the attachment of bacteria (May et al., 2016). We also showed that the surface chemistry of the black diamond needles can be tuned to further improve the killing efficiency and reduce adhesion (Dunseath et al., 2019). Superhydrophobic fluorine-terminated diamond surfaces, in particular, have proven to be effective in this regard. In our previous work, black diamond has proven to be a useful antibacterial surface for both Gram-negative and Gram-positive bacteria in static conditions and medically relevant strains (Dunseath et al., 2019; Norouzi et al., 2023).

These encouraging results suggest that black diamond surfaces might also prove useful in killing other micro-sized organisms, such as those responsible for marine biofouling. Such microorganisms (e.g. marine bacteria) initiate biofilm development and then ensure the film cohesion through the secretion of large amounts of Extracellular Polymeric Substances (EPS) (Lelchat et al., 2015; Mieszkin et al., 2013; Salta et al., 2013). As such, this work aimed to test black silicon and black diamond surfaces with different surface terminations for their efficacy in the prevention of marine biofilm formation. A major difference from our previous work is that, apart from using different organisms, bacterial adhesion was tested over longer periods (up to 7 weeks) and under hydrodynamic conditions that mimic marine environments.

2. Materials and methods

2.1. Surface samples

Flat silicon (Flat-Si) and flat diamond with hydrogenated or fluorinated surface termination (Flat-H and Flat-F, respectively) control samples were prepared as reported in Norouzi et al. (2023). Flat-Si was a standard polished Si(100) substrate. Note that as-grown silicon has a thin (10 nm) native oxide layer on its surface, resulting from oxidation by ambient air, which can decrease its hydrophobicity. For the flat diamond controls (Flat-H and Flat-F), Flat-Si substrates were first manually abraded using diamond powder (average size <3 μm) and then subjected to the same deposition conditions as the black diamond samples, except that the chemical vapour deposition (CVD) time was 6 h. This deposited a polycrystalline diamond film with a thickness of 3 ± 0.3 μm. Although we call these 'flat' samples, they have a surface roughness of ~0.3 μm due to the misorientation of the crystallite facets in the polycrystalline film.

Twelve-inch black silicon wafers were supplied by Lam Research Corporation (USA). They were fabricated using a reactive-ion etching method with a gas mixture of SF_6/O_2. This process resulted in sharp nanoneedles (or spikes) up to 10 μm in length, with a tip separation of 0.25–0.5 μm, as confirmed previously by Scanning Electron Microscopy (SEM) analysis (Dunseath et al., 2019). The bSi substrates were then mechanically cleaved into 5 mm × 5 mm pieces. Due to the etching process, these bSi samples will have a surface termination consisting of a mixture of O and F in unknown proportions. The O content will make these surfaces less hydrophobic than the 100% F-terminated bSi-F samples described later. Thus, we have labelled these pristine black silicon samples bSi-OF to emphasize that a mix of both O and F groups was present on the surface.

To fabricate the bD samples, the bSi samples were first submerged face-up in a colloidal nanodiamond suspension (average size 3.3 nm, NanoAmando, Japan) dispersed in methanol for 1 h. Due to electrostatic forces, the nanodiamond particles settled onto all surfaces of the bSi substrate, including the near vertical sides of the Si needles, forming a near continuous close-packed layer. These seeded substrates were then placed into a hot-filament CVD (HF-CVD) reactor. A gas mixture containing 1% CH_4 and 99% H_2 with a total gas flow of 202 sccm was used for the CVD growth. The chamber pressure was set to 20 Torr, while the Ta filament and substrate temperatures were fixed at ~2000°C and 900°C, respectively. A growth time of 30 min deposited a thin (~100-150 nm) conformal layer of nanocrystalline diamond onto the nanostructured surface, producing so-called 'black diamond' surfaces. The bD surfaces exhibited shorter, thicker needles with an increased tip radius compared to the original black silicon (bSi). These morphological changes resulted from the CVD process, which reduced the needle length to approximately 3–4 μm while simultaneously depositing a uniform and conformal diamond layer down to the base. Consequently, the needle tips became rounded, with an estimated tip radius of ~100 nm, while the spacing between adjacent tips (≈0.25–0.5 μm) was largely preserved. These morphological modifications demonstrate that the CVD process maintains the overall structure while altering the nanoscale tip geometry, which can significantly influence both mechanical and antimicrobial interactions with bacteria (Norouzi et al., 2023).

Because the CVD process gas mixture is predominantly hydrogen, the surface of any diamond films deposited is automatically mostly H-terminated (May, 2000). Nevertheless, to ensure the bD or flat diamond samples were completely hydrogen-terminated, the CH_4 supply was shut off 1 min before the completion of the process, allowing this final minute of processing to be performed in a pure H_2 atmosphere, leaving the as-grown diamond surfaces 100% hydrogenated.

To achieve fluorine-terminated surfaces, the flat and nanostructured control samples were further treated with SF_6 for 7-10 s in a DC plasma system to produce fluorinated versions: Flat-F, bSi-F and bD-F, respectively. Through this process, the C—H bonds on the exposed surfaces were replaced with C—F bonds, which imparted a high degree of hydrophobicity to the surfaces, as discussed previously (Norouzi et al., 2023). Table 1 summarises all the samples produced and tested in the present study.

Perspex and steel (1 cm^2; Neves & Neves, Lda, Portugal) were also used as reference substrates. Perspex is a polymer commonly used in submerged devices and marine equipment (e.g., hydrographic sensors, measuring instruments, underwater boat windows, and aquaculture systems) due to its high UV and chemical resistance, greater clarity compared to glass, lightweight nature, and ease of shaping and repair (Blain et al., 2004; King et al., 2004, 2006; Roy, 1994; Taylor, 1996). Steel is widely used in marine structures and equipment (e.g., boats, ship hulls, anchors, and offshore platforms) for its mechanical strength and durability (Harper et al., 2016; Mansour and Liu, 2008).

2.2. *Surface characterization*

The wettability of the materials was measured by static contact angles, and was performed by a 3 μL sessile water drop, measured at room temperature in ambient air with an in-house developed system (da Silva Domingues et al., 2013; van der Mei et al., 2002). The contact angles were calculated in degrees from gray-scale pictures obtained of the water droplets.

SEM analysis was performed to evaluate the morphology of the tested surfaces. The surfaces were sputter-coated with an EM ACE 600 (Leica Microsystems, Vienna, Austria) with a 4 nm layer of gold/palladium alloy and imaged with a Supra 55 Scanning Electron Microscope (Carl Zeiss, Oberkochen, Germany). Images were taken at magnifications of 10,000 × and 50,000 × at 3 kV, with the sample tilted at an angle of ~28°.

2.3. *Bacterial strain and culture conditions*

Gram-negative *Cobetia marina* was used to study the antifouling performance of the synthesized surfaces because this bacterium has been widely used in marine biofouling studies as a model biofilm-forming bacterium (Lima et al., 2022; Sousa-Cardoso et al., 2023). *C. marina* DSMZ 4741 was obtained from the Leibniz Institute DSMZ (German Collection of Microorganisms and Cell Cultures, Braunschweig, Germany) and originally isolated from a coastal sea sample at Falmouth, Massachusetts, USA (Arahal et al., 2002). *C. marina* was streaked onto Våatanen Nine Salt Solution (VNSS) medium (Mårdén et al., 1985), which mimics the nutritional conditions of marine environments, supplemented with 15 g/L agar (VWR International, Leuven, Belgium). Bacteria were grown for 24 h at 25 °C. Subsequently, individual colonies were transferred to 100 mL of fresh VNSS medium and incubated at 25 °C and 100 rpm in an orbital shaker (Agitorb 200ICP, Norconcessus, Ermesinde, Portugal). The bacterial culture was then centrifuged for 10 min at 3100 *g* (Eppendorf Centrifuge 5810R, Eppendorf, Hamburg, Germany) to form a pellet. This pellet was resuspended in fresh VNSS medium, and the cell suspension was adjusted to a final concentration of 3.5×10^7 cells/mL ($OD_{610nm} = 0.1$) using a V-1200 spectrophotometer (VWR International China Co., Ltd., Shanghai, China) before performing the biofilm assays.

Table 1
Description of control and active surfaces used in the study. The naming convention used is that H means hydrogenated and F means fluorinated.

Surface type	Surface code	Surface description
Controls	Flat-Si	Silicon control with a native oxide surface
	Flat-H	Flat diamond (continuous microcrystalline diamond film on a flat Si substrate) with H termination
	Flat-F	As Flat-H, but with F termination
Active surfaces	bSi-OF	Black silicon with native oxide termination
	bSi-F	Black silicon with F termination
	bD-H	Black diamond with H termination
	bD-F	Black diamond with F termination

2.4. *Biofilm formation assays*

Biofilm development was performed in a long-term assay under controlled hydrodynamic conditions to mimic marine environments (Romeu et al., 2019). Briefly, the biofilm formation assays were conducted using 12-well microtiter plates (VWR International, Carnaxide, Portugal), which were incubated at 25 °C and 185 rpm in a 25-mm-diameter orbital shaker (Agitorb 200ICP, Norconcessus, Ermesinde, Portugal). In this setup, an average shear rate of 40 s^{-1} was achieved at the beginning of biofilm formation (Romeu et al., 2019), which is similar to the values of shear rate to which a ship in a harbour is subjected (50 s^{-1}) (Alexandrou, 2001; Bakker et al., 2003). Additionally, this platform successfully replicated the observed biofouling behaviour during prolonged immersion of surfaces in the sea (Silva et al., 2021). Samples (approximately 1 cm^2) were carefully handled with the aid of tweezers to avoid touching, abrading, or damaging the spiky surfaces. These were sterilized by immersion in a 70% (*v*/*v*) ethanol solution (VWR International, Rosny-sous-Bois-cedex, France) for 2 min and allowed to dry in the flow chamber. After fixing the surfaces to the microplate wells with double-sided adhesive tape, 3 mL of the adjusted *C. marina* suspension was inoculated into each well. Since a 7 to 8-week interval for maintenance is the minimum duration for economically viable underwater monitoring systems (Blain et al., 2004; Faria et al., 2021; Romeu et al., 2019), biofilm development was performed for 7 weeks (49 days). During this incubation period, the medium was replaced twice a week. A total of four replicates (two biological assays with two technical replicates each) were analyzed.

2.5. *Biofilm analysis*

After 7 weeks of incubation, *C. marina* biofilms were analyzed for morphology by SEM, structure by Optical Coherence Tomography (OCT), spatial distribution of bacterial viability by Confocal Laser Scanning Microscopy (CLSM), number of total cells by flow cytometry (FC), and number of culturable cells by Colony-Forming Unit (CFU) counting. Additionally, the antibacterial mechanisms of action of the synthesized surfaces were characterized by FC.

SEM was also used to assess the effect of conditioning with the VNSS culture medium on surface morphology, as well as to examine the morphology of *C. marina* biofilms formed after 7 weeks of incubation. To evaluate surface conditioning and biofilm formation, surfaces were removed from the microtiter plates, dehydrated through a graded ethanol series (10%, 25%, 40%, 50%, 70%, 80%, 90%, and 100% (*v*/*v*)), and stored in a desiccator until imaging (Alves et al., 2020). All samples were then sputter-coated with a 4 nm layer of gold/palladium alloy using an EM ACE 600 (Leica Microsystems, Vienna, Austria) and imaged with a Supra 55 SEM (Carl Zeiss, Oberkochen, Germany) at magnifications of 10,000 × and 50,000 × times, using an accelerating voltage of 3 kV and at a tilted angle of approximately ~28°.

Several biofilm parameters, including biofilm thickness, contour coefficient, porosity, and the average size of non-connected pores, were evaluated by OCT. Briefly, the culture medium was carefully removed from the microplate wells and replaced with 3 mL of sterile sodium chloride solution (8.5 g/L) to eliminate loosely attached cells. Subsequently, two-dimensional (2D) and three-dimensional (3D) images of the *C. marina* biofilms that had formed on the different surfaces were acquired and analyzed as previously described (Faria et al., 2021; Romeu et al., 2019, 2022) using a Thorlabs Ganymede Spectral Domain OCT system with a central wavelength of 930 nm and a Thorlabs LSM03 objective scan lens (Thorlabs GmbH, Dachau, Germany). The imaging frequency used was 36 kHz, and the refractive index of the biofilm was set to 1.40, which is close to the refractive index of water (1.33). Representative sections of the entire coupon surface were chosen arbitrarily. For each coupon, 2D and 3D imaging were performed with a minimum of 3 fields of view to ensure the reliability and accuracy of the results obtained. The captured volume was ~$3 \times 2 \times 2$ mm^3 ($509 \times 313 \times 1024$ pixels^3). For image analysis, the base of the biofilm was determined by fitting a parabola and a hyperboloid to the 2D and 3D images, respectively, connecting the white pixels from light reflection on the substratum surface. A Gray-value threshold to distinguish the biofilm from the background was set based on the Gray-value histogram of the entire selected region of interest (Otsu, 1979). The upper contour of the biofilm was defined as the pixel farthest from the bottom with gray values above the threshold and connected to the biofilm base. Objects not connected to the base were excluded from biofilm structure analysis. The biofilm thickness, contour coefficient, porosity, and average size of the non-connected pores were assessed as detailed in Romeu et al. (2022). A summary of the parameter definitions and equations is presented in Table S1. The average size of non-connected pores inside the biofilm structure was quantified, assuming a minimum size of non-connected pores equal to 1000 μm^3 and defining a voxel size of 1 as corresponding to 117 μm^3 (Romeu et al., 2022). The values of the total biofilm volume and volume of non-connected pores at different positions, i, along the biofilm thickness L_{F_i} (from $i = 0$ to the maximum biofilm thickness) obtained for each field of view, were used as cumulative values. Therefore, the final values of these parameters were represented as the values achieved at the maximum biofilm thickness.

The cell viability and spatial organization of biofilms formed on the tested surfaces were assessed by CLSM after staining with the Live/Dead® BacLight bacterial viability kit (Invitrogen Life Technologies, Alfagene, Portugal) for 10 min in the absence of light (Gomes et al., 2022). This kit is composed of two nucleic acid-binding stains: SYTO 9 (green), which enters all bacteria, and propidium iodide (PI, red), which only enters bacteria with compromised cell membranes. The biofilm analysis was performed using a Leica DMI6000-CS inverted microscope (Leica Microsystems, Wetzlar, Germany) equipped with a × 40 water immersion objective (Leica HCX PL APO CS; Leica Microsystems). SYTO 9-stained bacteria were detected using a 488 nm argon laser and a 500–550 nm bandpass emission filter, while PI-stained bacteria were detected using a 633 nm helium-neon laser and a 610–680 nm bandpass emission filter. A minimum of five stacks (387.5 μm × 387.5 μm) with a z-step of 1 μm were recorded for each biofilm sample. 3D projections and 2D sections of the biofilm samples were obtained using the IMARIS 9.3 software (Bitplane AG, Zurich, Switzerland). Total biofilm biovolume (μm^3/μm^2) was extracted from CLSM stacks using COMSTAT2 (Heydorn et al., 2000), and biofilm viability was expressed as the percentage of viable biovolume relative to the total biovolume. The viable biovolume was estimated by subtracting the red-channel signal (non-viable cells) from the green-channel signal (all cells). The intensity values of both fluorescence signals relative to the z-position were traced using the Stack Profile tool provided by the LAS AF Lite software (Leica Microsystems, Wetzlar, Germany).

To quantify the number of total cells in the biofilms formed on the different surfaces, each surface was removed from the microplate wells and immersed in 2 mL of sterile saline solution (8.5 g/L). The surfaces were vortexed for 3 min to detach the adhered bacteria (Romeu et al., 2019). The number of total cells per cm^2 was determined through FC, acquiring 10 μL of the cell suspension at a flow rate of 10 μL/min (CytoFLEX V0-B3-R1, Beckman Coulter, Brea, CA, USA). The number of biofilm culturable cells was assessed by spreading the bacterial suspensions on VNSS agar plates, followed by overnight incubation at 25 °C for CFU counting. Culturability (%) was defined as CFU divided by total cell count from FC.

2.6. *Characterization of the mechanisms of action of the synthesized surfaces*

The mechanisms of action of the tested surfaces were characterized by flow cytometry. Briefly, *C. marina* cells (3.5×10^7 cells/mL) were exposed to the surfaces for 24 h at 25 °C. The surfaces were then immersed in 2 mL of sterile saline solution (8.5 g/L) and vortexed for 3 min to detach adhered bacteria. Bacterial membrane potential, enzymatic activity, and the production of reactive oxygen species (ROS) were assessed by staining the cells with *bis*(1,3-dibutylbarbituric acid) trimethine oxonol (DiBAC$_4$(3); Sigma-Aldrich, Taufkirchen, Germany) at 0.5 μg/mL, 5(6)-carboxyfluorescein diacetate (CFDA; Sigma-Aldrich, Taufkirchen, Germany) at 5 μg/mL, and 2′,7′-dichlorofluorescein diacetate (DCFH-DA, Sigma-Aldrich, Taufkirchen, Germany) at 10 μM, respectively (Lima et al., 2022; Sousa-Cardoso et al., 2023). Cells were stained for 30 min in the absence of light and analyzed using a CytoFLEX flow cytometer model V0-B3-R1 (Beckman Coulter, Brea, CA, USA). Bacteria were gated based on forward-scatter (FSC) and side-scatter (SSC) signals and acquired at a flow rate of 30 μL/min. The results were analyzed using CytExpert software (version 2.4.0.28, Beckman Coulter, Brea, CA, USA) and presented as the mean intensity of fluorescence (MIF) at 525/40 nm for DiBAC$_4$(3), CFDA, and DCFH-DA. Two independent assays were performed.

2.7. *Seawater exposure tests*

Surface exposure tests were performed using real seawater on the four active surfaces (bSi-OF, bSi-F, bD-H, and bD-F), the control surface (Flat-Si), and two materials commonly used in marine environments with different nature: a metallic (steel) and a polymer substrate (Perspex). Seawater was collected at Homem do Leme beach (41.160610 N, 8.686230 W), Porto, Portugal. Biofilm formation under controlled hydrodynamic conditions mimicking marine environments was performed as described in Section 2.4. Three mL of seawater were added to each well, and biofilms were allowed to develop over 4 weeks, with seawater replaced twice weekly. After incubation, biofilms were analyzed for their structure using OCT and SEM, as detailed in Section 2.5. Experiments were conducted in triplicate.

2.8. *Statistical analysis*

The D'Agostino-Pearson and Shapiro-Wilk normality tests were performed to check if the data presented a normal distribution. Differences between biofilm thickness, contour coefficient, porosity, and average size of non-connected pores were evaluated using the unpaired, non-parametric Mann-Whitney test in GraphPad Prism® for Windows, version 6.01 (GraphPad Software, Inc., San Diego, CA, USA) since the variables were not normally distributed. Differences between biovolume and total cells were compared using one-way analysis of variance (ANOVA) in IBM SPSS Statistics version 24.0 for Windows (IBM SPSS, Inc., Chicago, IL, USA). The error bars in the graphs correspond to the standard deviation (SD) of the mean, except for the percentages of biofilm viability and culturability, for which the error bars were obtained using the error propagation method. Statistically significant differences were considered for p values < 0.05 (corresponding to a confidence level greater than 95%).

3. Results and discussion

3.1. Surface characterization

In this study, the antifouling potential of the spiky hydrogen- and fluorine-terminated bSi and bD surfaces was assessed against a 7-week-old biofilm of *C. marina* formed under hydrodynamic conditions mimicking those found in marine environments. Since bacterial adhesion and biofilm development are affected by surface properties (Zheng et al., 2021), the contact angle (θ_W) between water and the tested surfaces was measured to assess their wettability. The θ_W values (Table 2) indicated that the Flat-Si (control surface) was the only surface that presented a hydrophilic character ($\theta_W < 90^\circ$), which is associated with high wettability, and is due to the native oxide layer mentioned earlier. This value is similar to that obtained for Perspex ($\theta_W = 73^\circ \pm 3^\circ$) (Romeu et al., 2019), which was also used as a reference material in this study. In general, the control surfaces were more wettable than the active surfaces (Table 2). Flat-H, Flat-F, and bSi-F surfaces displayed lower wettability than Flat-Si ($98^\circ \pm 4^\circ$, $107^\circ \pm 3^\circ$, and $106^\circ \pm 3^\circ$, respectively), followed by bSi-OF and bD-H spiky surfaces ($115^\circ \pm 1^\circ$ and $122^\circ \pm 1^\circ$, respectively). The bD-F surface showed the lowest wettability, with a water contact angle of $132^\circ \pm 1^\circ$. Overall, the θ_W values increased from flat to spiky topographies, and within the spiky surfaces, from non-coated to diamond-coated ones, showing a progressive reduction in surface wettability. Additionally, a greater increase in θ_W was observed on the bD surfaces, from 122° (H-terminated) to 132° (F-terminated). As reported in a previous study (Norouzi et al., 2023), the replacement of H with F bonds provides a more hydrophobic nature to the surface, which is consistent with our observations.

Because a previous study showed that *C. marina* has a hydrophilic nature ($\theta_W = 37^\circ \pm 2^\circ$) (Sousa-Cardoso et al., 2023), its adhesion to more hydrophobic surfaces is expected to be less thermodynamically favorable, particularly when surface energy mismatch and roughness are considered (Hermansson, 1999; Oh et al., 2018).

SEM was first employed to analyze the surface morphology of control and active surfaces (Fig. 1). The pristine Flat-Si samples showed a surface that was smooth on the nm scale, with a few nm-sized scratches resulting from handling. The Flat-H and Flat-F surfaces are indistinguishable, suggesting that the fluorination procedure did not significantly etch the diamond surface. They both exhibited faceted diamond microcrystallites of 1-2 μm in size, randomly oriented with respect to one another, and with atomic-scale grain boundaries between the crystals. This is typical of a microcrystalline diamond film. Although we refer to these samples as ‘flat’ diamond, they have a root mean square (RMS) roughness of around 0.3 μm due to the misorientation of the crystallite facets.

The bSi-OF and bSi-F surfaces featured dense arrays of vertically aligned high-aspect-ratio Si microneedles. These sharp, spike-like structures were morphologically consistent between OF- and F-terminated variants, again highlighting that the fluorination process does not etch the Si spikes. In contrast, the bD-H and bD-F surfaces showed rounded, dome-like nanostructures resembling blunted needles because of the diamond coating. Compared to bSi, the surface of these needles appears rougher due to the presence of the thin nanocrystalline diamond coating, potentially enhancing their antifouling performance by further reducing the effective contact area.

Table 2
Water contact angles of the surfaces used in this study.

Surfaces		Water Contact Angles ($\theta_{W,}$ ^{0})
Controls	Flat-Si	69 ± 5
	Flat-H	98 ± 4
	Flat-F	107 ± 3
Active surfaces	bSi-OF	115 ± 1
	bSi-F	106 ± 3
	bD-H	122 ± 1
	bD-F	132 ± 1

Therefore, the combination of high contact angles and nanoscale roughness on surfaces like bSi-OF, bD-H, and bD-F may contribute to reduced biofilm formation by limiting effective bacterial contact with the surface or promoting detachment.

3.2. Biofilm analysis

The formation of a conditioning film resulting from the adsorption of molecules from the surrounding environment can influence biofilm development. Thus, surface morphology was also analyzed by SEM after incubation with culture medium alone, and images show salt crystals, inorganic residues, and protein deposits on all surfaces (Fig. 2A). Flat-Si and Flat-H showed more noticeable accumulations than the remaining surfaces, where a thin film or scattered residues were observed, often outlining surface features. The spiky structures of both bSi (-OF and -F) and bD (-H and -F) retained their sharp morphology despite slight surface fouling.

Protein adsorption assays (Section 2 of Supplementary Material), using casein as a model protein, confirmed that Flat surfaces accumulated protein, whereas bSi and bD surfaces stayed mostly clean (Figs. S1 and S2), consistent with the previous results from VNSS conditioning.

After biofilm formation, surfaces showed variable levels of biofilm coverage and architecture (Fig. 2B). Flat-Si, Flat-H, Flat-F, and bD-H surfaces were fully covered with biofilm. In contrast, the nanostructured bSi-OF, bSi-F, and bD-F did not show complete biofilm coverage after 7 weeks of incubation. Several regions remained uncolonized, and the surface nanostructures were still clearly distinguishable. In some areas, the nanoneedles were observed piercing through the biofilm matrix, indicating that the surface topography may have interfered with uniform biofilm development and possibly contributed to mechanical disruption of cell attachment.

Different surfaces may trigger diverse biofilm structures, including the distribution of interstitial pores, which, in turn, affect their resistance to mechanical or chemical challenges, and facilitate water and nutrient transport (Bas et al., 2017; Peterson et al., 2015, 2021). Accordingly, *C. marina* biofilms were further analyzed by OCT to quantify biofilm thickness, contour coefficient, porosity, and the average size of non-connected pores (Fig. 3). Additionally, Figs. 4 and 5 present 3D and 2D OCT images of 7-week-old *C. marina* biofilms, respectively.

The average thickness of biofilms developed on Flat-Si (control surface) was 140 ± 46 μm (Fig. 3A). Biofilms formed on Flat-H, Flat-F, bD-H, and bSi-F surfaces were similar in thickness to those formed on Flat-Si ($p > 0.05$). In contrast, the thickness of *C. marina* biofilms formed on bSi-OF and bD-F decreased by 53% and 51% ($p < 0.05$), respectively, compared to biofilms formed on Flat-Si. Similarly, regarding the contour coefficient (Fig. 3B), Flat-Si, Flat-H, Flat-F, bD-H, and bSi-F surfaces exhibited higher values than bSi-OF and bD-F surfaces. Since this biofilm parameter indicates the portion of the biofilm that is exposed to the surrounding medium (values close to 1 reflect a flat biofilm, while values higher than 1 represent biofilms with heterogeneous structures (Romeu et al., 2022)), it was possible to observe that biofilms developed on bSi-OF and bD-F surfaces were smoother and more homogeneous than the biofilms formed on the remaining surfaces. Moreover, the highest value of contour coefficient achieved on Flat-Si (7.6 ± 0.9) demonstrated the ability of this surface to potentiate the development of a more heterogeneous biofilm architecture. The 3D OCT representative images in Fig. 4 support these quantitative data. Indeed, biofilms formed on the control surfaces (Flat-Si, Flat-H, and Flat-F) exhibited greater thickness, while a marked decrease was evident on both the bSi-OF and bD-F surfaces (Fig. 4). Furthermore, biofilms formed on Flat-Si had a truly heterogeneous architecture, supporting the high contour coefficient seen in Fig. 3B. This surface presented large biofilm streamers on

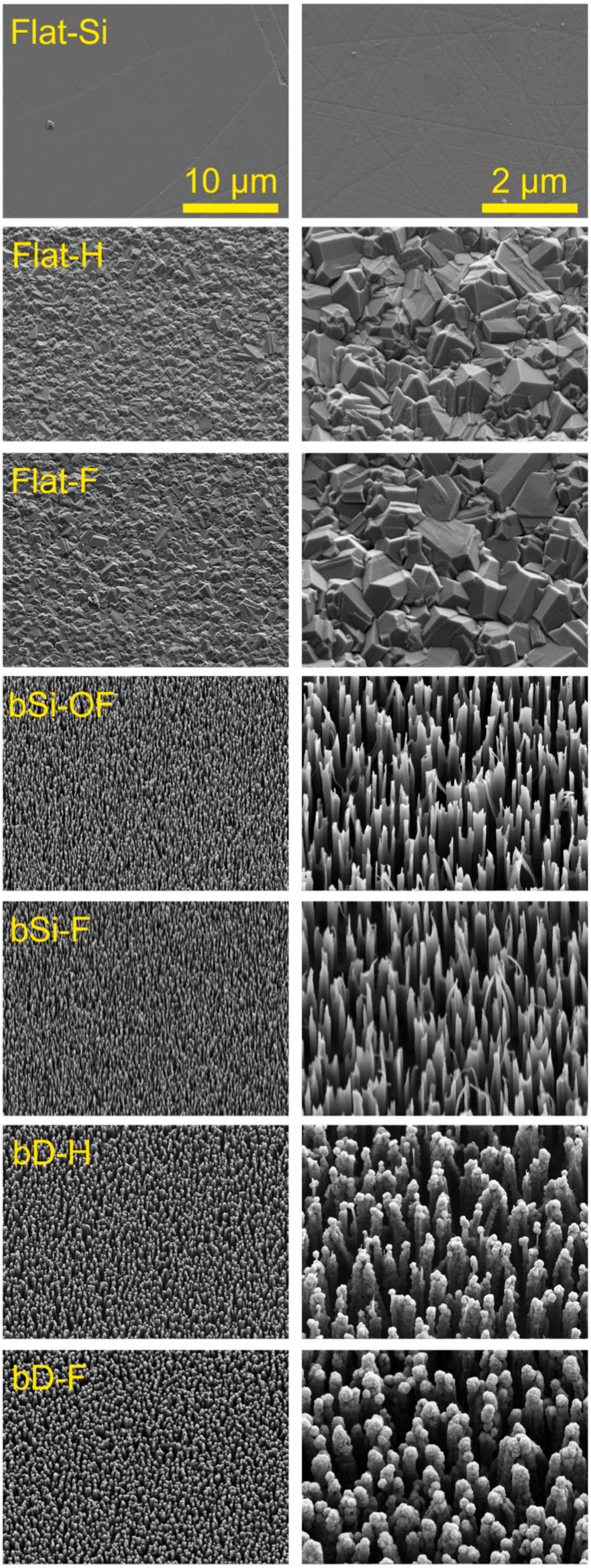

(caption on next column)

Fig. 1. SEM micrographs of pristine surfaces used to evaluate their morphology. The left panels show the overall surface topography at 10,000 × magnification (scale bar = 10 μm), while the right panels provide higher-resolution details at 50,000 × magnification (scale bar = 2 μm). These images confirm the smooth surface of Flat-Si samples and the presence of randomly oriented diamond microcrystallites in Flat (-H and -F) surfaces. In contrast, bSi (-OF and -F) surfaces exhibit vertically aligned, high-aspect-ratio microneedles, whereas bD (-H and -F) surfaces show rounded needles on the top.

the biofilm structure, reaching up to 300 μm. These structures were also observed on the other tested surfaces, albeit with reduced thickness or quantity. These large streamers may affect local hydrodynamics (Romeu et al., 2024) and increase the surface area of the biofilm exposed to the surrounding environment, thereby enhancing the access of nutrients and oxygen to the inner biofilm cells and promoting its growth (Romeu et al., 2019, 2022). The maximum values obtained for biofilm porosity and the average size of non-connected pores were also observed on the Flat-Si surface (15% and 3460 μm^3, respectively; Fig. 3C and D). The biofilm porosity decreased by 32% to 65% on the Flat-H, bSi-OF, bSi-F, and bD-F surfaces compared to the Flat-Si control ($p < 0.05$, Fig. 3C). However, no significant differences in biofilm porosity were found between H-/OF-terminated surfaces and their corresponding F-terminated counterparts. In contrast, regarding the average size of non-connected pores (Fig. 3D), the Flat-H and bSi-OF surfaces demonstrated a decrease of 25% and 32% ($p < 0.05$), respectively, compared to their corresponding F-terminated counterparts, namely Flat-F and bSi-F. Furthermore, on the Flat-H, bSi-OF, and bD-F surfaces, a reduction in the size of non-connected pores of 32%, 36%, and 42% ($p < 0.05$), respectively, was observed compared to Flat-Si. The 2D OCT images in Fig. 5 corroborate the quantitative data on biofilm porosity and the average size of non-connected pores depicted in Fig. 3C and D. Indeed, biofilms formed on Flat-Si showed a higher porosity (represented in yellow), while biofilms developed on Flat-H, bSi-OF, bSi-F, and bD-F exhibited minor fractions. Similarly, Fig. 5 shows that Flat-Si exhibited the largest size of non-connected pores, followed by bSi-F, Flat-F, bD-H, Flat-H, and bSi-OF. The spiky bD-F surface had the smallest non-connected pores. The lower porosity and smallest average size of non-connected pores of biofilms formed on the bD-F surface may reduce the viability of cells in the deepest layers of the biofilm, as mass transfer to the inner regions of the biofilm may be decreased.

To gain a deeper insight into the impact of modified silicon surfaces on biofilm structure and viability, CLSM analysis was performed (Figs. 6 and 7A). Fig. 6 shows a representative 3D aerial reconstruction (left; the shadow projections on the right side of these images represent the biofilm thickness) and a corresponding cross-sectional side view (middle) of the biofilms developed on the control and active surfaces. Additionally, a normalized fluorescence intensity histogram (right) illustrates the vertical (*z*-axis) distribution of green and red fluorescence signals, offering a detailed depiction of the spatial organization and depth of the viable (live) and non-viable (dead) biofilm fractions.

Biofilms formed on Flat-Si demonstrated a dense and thick structure (as shown by the shadow projection), confirming the previous results obtained from OCT (Fig. 3A, 4 and 5). Moreover, a co-localized distribution of viable and non-viable cells throughout the biofilm was evident for this control surface. Although there was some cell death, the overall viability of biofilm cells remained high on this relatively inert surface (Fig. 6).

On hydrogenated surfaces (Flat-H, bSi-OF, and bD-H), biofilm development was notably more pronounced than on their fluorinated counterparts (Flat-F, bSi-F, and bD-F). The Flat-H surface exhibited the thickest biofilm among the hydrogenated surfaces (as shown by the shadow projection), followed by bSi-OF, which supported moderate biofilm development, and bD-H, which showed the lowest overall biomass.

In terms of cell viability, all three hydrogenated surfaces displayed

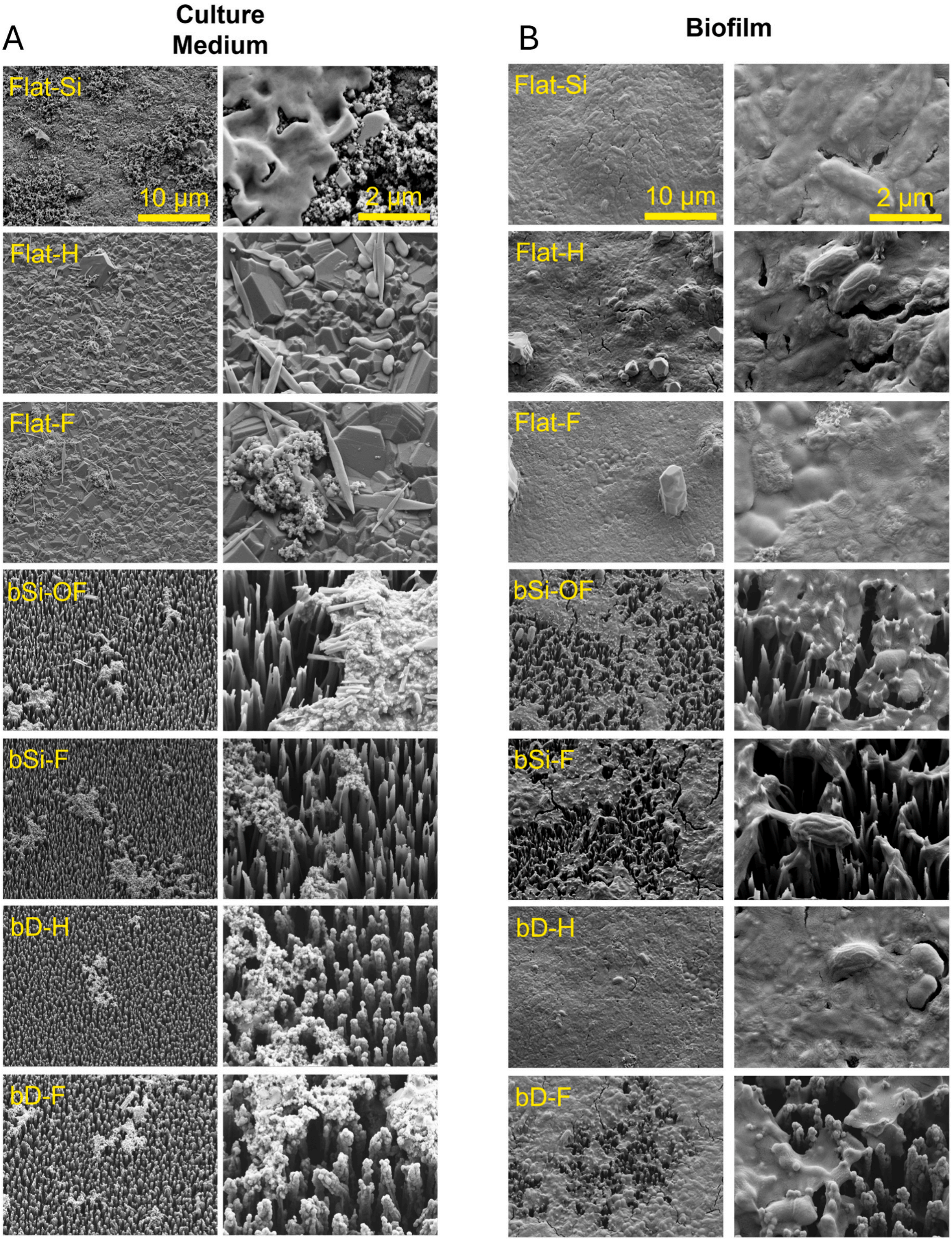

Fig. 2. SEM micrographs of the different surfaces after exposure to (A) culture medium and (B) biofilm-forming conditions. At 10,000 × magnification (left images, scale bar = 10 μm), the overall surface morphology is visible, while at 50,000 × magnification (right images, scale bar = 2 μm), finer details can be observed. After culture medium exposure (A), although deposits are present on all surfaces, Flat surfaces show higher accumulation. The spiky structures of bSi and bD preserve their morphology. After biofilm development (B), Flat (-Si, -H, and -F) and bD-H surfaces are fully covered, whereas bSi (-OF and -F) and bD-F surfaces retain several uncolonized regions.

comparable levels of red fluorescence, suggesting a similar proportion of non-viable cells. However, differences were observed in the spatial distribution of these non-viable cells. On both Flat-H and bSi-OF, the green and red fluorescence intensity profiles overlapped throughout the biofilm depth. In contrast, on bD-H, the peak of red fluorescence was concentrated closer to the surface, indicating that cell death was primarily localized in the deeper layers of the biofilm. This suggests that the bactericidal effect of the nanostructured bD-H surface was most

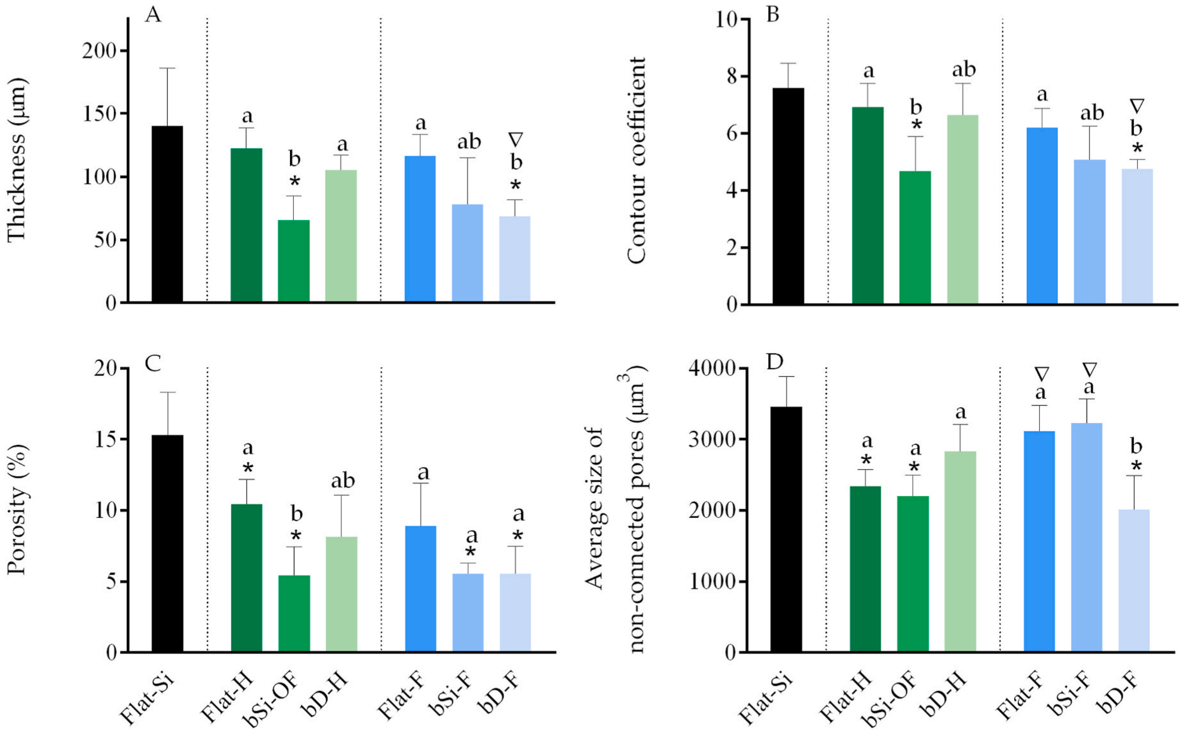

Fig. 3. *C. marina* biofilm development after 7 weeks on control (Flat-Si), and flat diamond, bSi and bD, H- and F- terminated. The analyzed parameters refer to biofilm thickness (A), contour coefficient (B), biofilm porosity (C), and average size of non-connected pores (D). Mean values and SD from two independent biological assays with two technical replicates each are represented. The black asterisk indicates significant differences between Flat-Si (control surface) and the modified surfaces. Significant differences between H-/OF-terminated surfaces (Flat-H, bSi-OF and bD-H), and between F-terminated surfaces (Flat-F, bSi-F and bD-F) are represented by different lowercase letters. The symbol ∇ represents significant differences between Flat-H *vs* Flat-F, bSi-OF *vs* bSi-F, and bD-H *vs* bD-F. All significant differences were considered for p values < 0.05 (unpaired, non-parametric Mann-Whitney test).

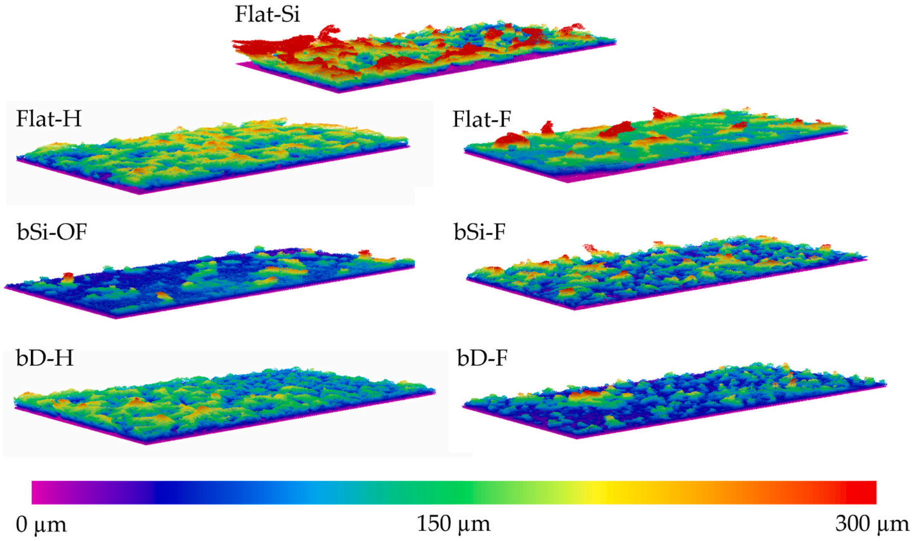

Fig. 4. Representative 3D cross-sectional OCT images of *C. marina* after 7 weeks of biofilm development on different surfaces: control (Flat-Si), flat diamond (Flat-H and Flat-F), bSi (-OF and -F), and bD (-H- and -F) surfaces. The colour scale represents the biofilm thickness (up to 300 μm). Thicker and more heterogeneous biofilms are observed on Flat-Si surfaces, whereas thinner biofilms are detected on bSi-OF and bD-F surfaces.

pronounced at the biofilm-surface interface.

Fluorinated surfaces showed a marked reduction in biofilm thickness and biomass, regardless of surface topography and chemistry. Similar to the trend observed for hydrogen-terminated surfaces, the Flat-F surface supported the thickest and most heterogeneously distributed biofilm among the fluorinated samples, followed by bSi-F. The most pronounced antimicrobial effect occurred on bD-F, where the biofilm was not only thinner, as visualized by OCT (Figs. 4 and 5), but also dominated by non-viable cells. Furthermore, on this surface, the peak of red fluorescence intensity was located near the base of the biofilm, indicating that the killing effect was more pronounced on *C. marina* cells residing in the inner layers of the biofilm, in close proximity to the substrate. CLSM imaging suggested that both bD-H and bD-F surfaces have an increased potential to reduce the viability of cells located at the bottom of the

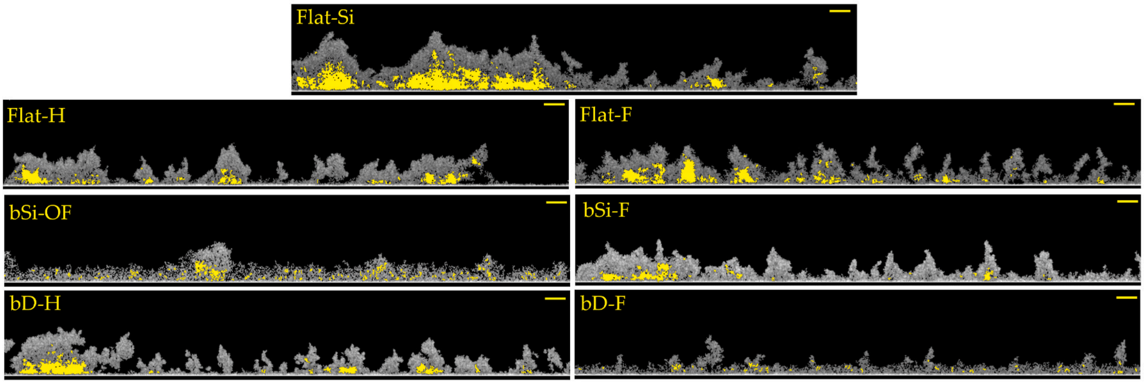

Fig. 5. Representative 2D cross-sectional OCT images of *C. marina* after 7 weeks of biofilm development on different surfaces: control (Flat-Si), flat diamond (Flat-H and Flat-F), bSi (-OF and -F), and bD (-H- and -F) surfaces. The biofilm biomass is represented in gray, and the empty spaces in the biofilm structure are highlighted in yellow (scale bar = 100 μm). Biofilms formed on Flat-Si exhibit the highest porosity, whereas those developed on bSi (-OF and -F) and bD-F surfaces display lower porosity.

biofilm. This effect is likely due to the mechanical robustness conferred by the thin diamond coating on the nanoneedles, which may increase physical stress on sessile cells at the biofilm-surface interface and thereby contribute to the overall antifouling performance of these surfaces.

Quantitative results of biofilm biovolume and biofilm viability (%) on the different surfaces, as presented in Fig. 7A, were derived from CLSM imaging analyses and further support the qualitative observations shown in Fig. 6. Among all surfaces, the unmodified Flat-Si and both flat diamond surfaces (Flat-H and Flat-F) exhibited the highest biofilm biovolumes ($\geq$100 $\mu m^3/\mu m^2$, Fig. 7A). Significant reductions in biofilm biovolume were observed on bSi-OF and bSi-F ($\sim$45%), with even more pronounced reductions on the diamond-coated surfaces bD-H and bD-F compared to the control surfaces ($p < 0.05$). More specifically, biofilms formed on bD-H showed a 61% reduction in total biovolume compared to Flat-H, while bD-F exhibited a 75% decrease relative to Flat-F. In parallel with the reduction in biovolume, most surfaces showed a tendency toward lower biofilm viability compared to the Flat-Si control (Fig. 7A), with a pronounced decrease on Flat-H, bD-H, and especially bD-F, where viable cells represented only 45% of the total biovolume.

Fig. 7B presents the total number of biofilm cells quantified by flow cytometry, and their culturability, calculated as the percentage of CFUs relative to total cell counts. Flat-Si was the surface with the highest biofilm cell density ($\sim 8.0 \times 10^8$ cells/cm^2), aligning with its high biovolume shown in Fig. 7A. However, a noticeable mismatch between biofilm biovolume (Fig. 7A) and cell number (Fig. 7B) was observed for some surfaces, which may be explained by differential production of EPS. Certain nanotopographies, particularly bD-H and bSi-F, exhibit a higher number of cells but likely reduce the secretion of extracellular matrix components, resulting in biofilms of lower volume. Such a response is characteristic of bacterial adaptation to physical stress induced by specific surface features (Mitik-Dineva et al., 2009; Zhang et al., 2018), which can alter the attachment behaviour and biofilm architecture. Despite these variations, bD-F consistently demonstrated reduced biovolume and cell density, underscoring its robust anti-biofilm performance.

The trend observed for biofilm culturability (Fig. 7B) is somewhat similar to that of biofilm viability (Fig. 7A), indicating a correlation between the ability of cells to form colonies and their viability within the biofilm. Culturability values for bD-F and bD-H were below 40%, reflecting a marked decrease in viable cells under culturable conditions.

As mentioned in Section 2.1, black silicon (bSi) exhibits needle-like features with sharp tips, whereas black diamond (bD) presents shorter, thicker needles with an increased tip radius. The flat diamond control samples (Flat-H and Flat-F), while lacking nanoscale protrusions, are not as smooth as Flat-Si (polished to a roughness of a few nm) due to the presence of misaligned polycrystalline diamond grains. These morphological differences are directly linked to bactericidal and antifouling performance. Consistent with this, Gorth et al. (2012) observed that sharp grain edges on Si_3N_4 can induce bacterial lysis, indicating that nanopillars are not the only nanofeatures capable of damaging bacterial cell walls. They compared smooth polished Si_3N_4 with as-fired Si_3N_4, which exhibits sharp grain-edge features similar to the Flat diamond samples used in the present work, and concluded that polished Si_3N_4 supported higher bacterial activity, whereas as-fired Si_3N_4 induced more cell lysis (Gorth et al., 2012). Increasing the roughness further, in the form of sharp, high-aspect-ratio needles of black silicon, enables strong mechanical disruption of bacterial membranes, while the thicker, blunter tips of bD may reduce puncture efficiency but improve surface robustness and durability. Moreover, the intrinsic chemical bonding plays a key role in determining the antifouling performance of the surfaces. While hydrogen termination imparts hydrophobicity and stabilizes the diamond surface, C-H bonds are relatively unstable in aqueous and biological environments, where partial oxidation or substitution can occur. This leads to surface heterogeneity and increased surface energy, promoting bacterial adhesion. In contrast, fluorine termination forms stronger and more chemically robust C-F bonds. The larger atomic radius of fluorine produces a densely packed surface that shields underlying carbon atoms, prevents interactions with the environment, reduces surface energy, and generates stronger electrostatic repulsion between adjacent fluorine atoms, as demonstrated in atomistic simulations (Sen et al., 2009). Experimental studies on fluorinated diamond-like carbon coatings have also shown significantly reduced bacterial adhesion and biofilm formation, confirming the superior antibacterial performance of fluorine-terminated coatings (Yonezawa et al., 2020).

To validate the antifouling performance of these engineered surfaces, biofilm formation on a Perspex substrate, one of the reference controls, was also evaluated (Section 3 of Supplementary Material). The average biofilm thickness on Perspex reached approximately 200 μm, while the Flat-Si control surface and bD-F (the most promising antifouling and antimicrobial surface) showed reductions of 26% and 64%, respectively, with the latter achieving a statistically significant decrease ($p < 0.05$, Fig. S3A). Regarding total bacterial cell numbers, reductions of 43% and 64% were observed on Flat-Si and bD-F, respectively, compared to Perspex ($p < 0.05$, Fig. S3B). Additionally, bD-F induced a reduction of about 30% in biofilm culturability relative to Perspex (Fig. S3B). These results demonstrate the enhanced antifouling and antimicrobial performance of the fluorine-terminated nanostructured surface when compared to a standard marine-relevant material.

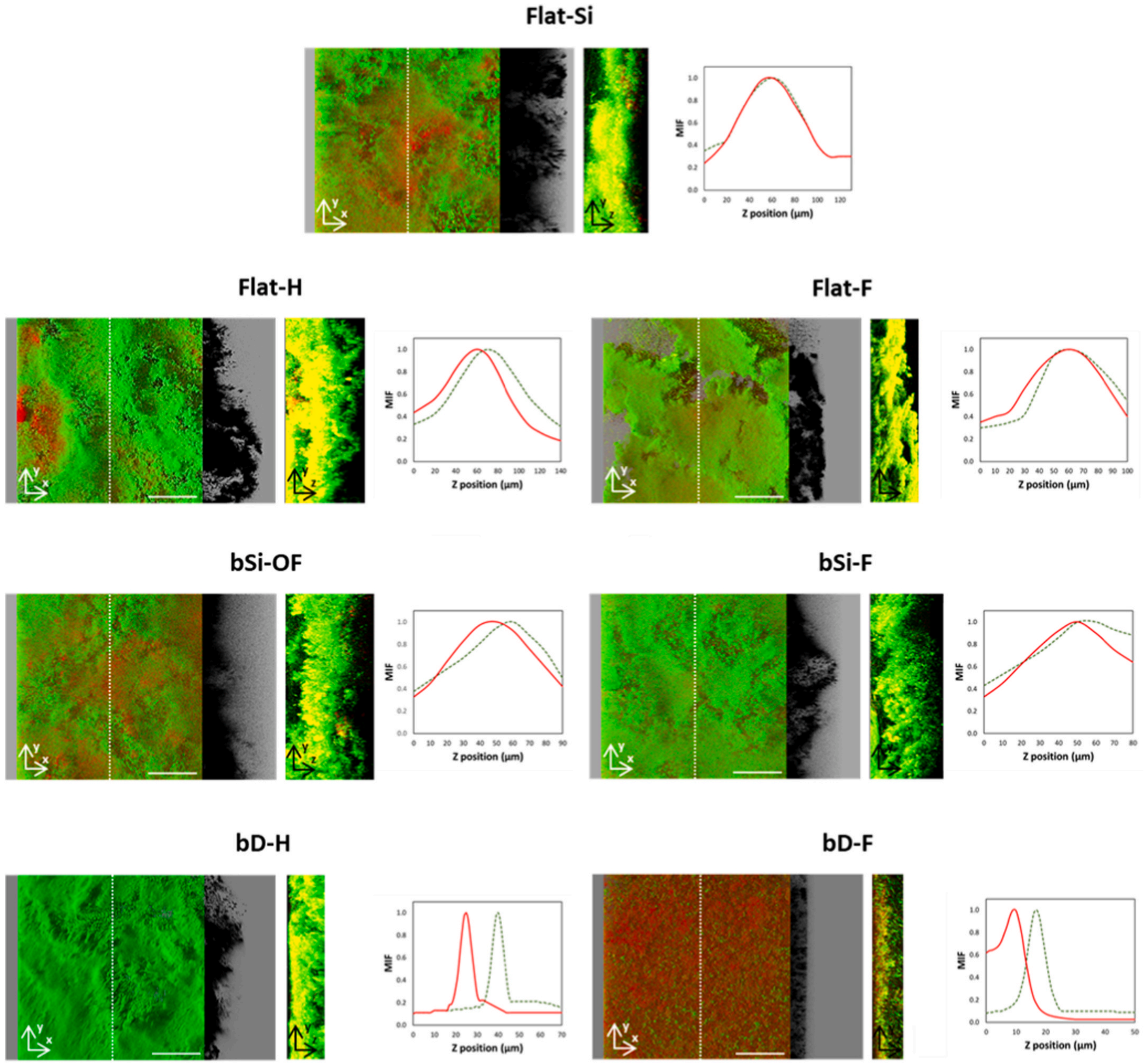

Fig. 6. Confocal microscopy analysis of 7-week-old *C. marina* biofilms for the assessment of bacterial cell viability on control (Flat-Si), flat diamond (Flat-H and Flat-F), bSi (-OF and -F), and bD (-H- and -F) surfaces. Viable and non-viable cells are shown in green (SYTO 9) and red (propidium iodide, PI), respectively. Representative images in the leftmost and middle panels were obtained from confocal *z*-stacks. The left panels display a 3D aerial view of the biofilm structure, in which the black shadow projection on the right side illustrates the biofilm thickness, whereas the middle panels show a cross-section slice of the biofilm along the white dotted line indicated in the aerial view (scale bar = 50 μm). Histograms in the right panels represent the distribution of normalized green and red fluorescence intensity, expressed as mean intensity of fluorescence (MIF) along the vertical (*z*) axis, indicating the depth-dependent distribution of viable (— green fluorescence signal) and non-viable (— red fluorescence signal) cells within the biofilm. Whereas Flat-Si shows a dense biofilm with co-localized viable and non-viable cells, fluorinated surfaces exhibit reduced biomass, and bD surfaces decrease cell viability at the biofilm bottom.

3.3. Characterization of the mechanisms of action of the synthesized surfaces

To further understand the mechanisms behind these effects, the impact of the tested surfaces on *C. marina* cells was evaluated by flow cytometry after 24 h of growth using different dyes (Fig. S4 in Supplementary Material). The data indicate that diamond surfaces change the bacterial membrane potential, as demonstrated by DiBAC$_4$(3) staining. This effect was more pronounced in bacteria grown on bD surfaces with needles (bD-H and bD-F), which exhibited higher MIF values – 2.9- and 3.7-fold higher than those grown on the Flat-Si control and 1.9- and 1.7-fold higher than those on the diamond controls (Flat-H and Flat-F, respectively). In turn, bacteria grown on bSi surfaces displayed slightly higher MIF values compared to those grown on the Flat-Si control, particularly on fluorine-terminated surfaces (bSi-F; 1.5-fold higher MIF). Additionally, needle-covered surfaces (both bSi and bD) appear to reduce the bacterial enzymatic activity, as revealed by CFDA cell staining. On hydrogen-terminated surfaces, bacteria grown on bSi-OF and bD-H surfaces exhibited 1.6- and 1.9-fold reductions in MIF, respectively, compared to those grown on Flat-Si. Similarly, on fluorine-

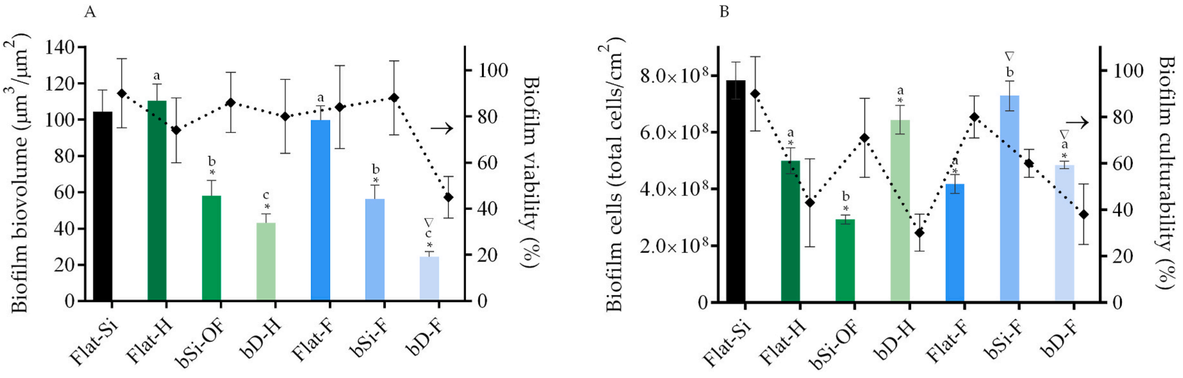

Fig. 7. (A) Total biovolume of *C. marina* biofilms after 7 weeks of biofilm development on different surfaces (bars), with the corresponding biofilm viability (%) indicated by the black dotted line and the right axis. (B) Total number of biofilm cells (bars), and biofilm culturability (%) shown by the black dotted line and the right axis. Mean values and SD or standard error from two independent biological assays with two technical replicates each are represented. The black asterisk indicates significant differences between the Flat-Si (control surface) and the modified surfaces. Significant differences between H-/OF-terminated surfaces (Flat-H, bSi-OF and bD-H), and between F-terminated surfaces (Flat-F, bSi-F and bD-F) are represented by different lowercase letters. The symbol ∇ represents significant differences between Flat-H *vs* Flat-F, bSi-OF *vs* bSi-F, and bD-H *vs* bD-F. All significant differences were considered for p values < 0.05 (ANOVA).

terminated surfaces, the MIF values were reduced by 2.2-fold on bSi-F and 1.9-fold on bD-F surfaces.

Regarding ROS production assessed by DCFH-DA staining, the data indicated that under the tested conditions, neither bSi nor bD surfaces induced ROS generation compared to the Flat-Si control. In fact, the MIF values of cells cultured on bSi (-OF and -F) and Flat (-H and -F) surfaces were comparable to those of cells grown on Flat-Si, with the exception of cells in contact with bD-H and bD-F surfaces, which exhibited reduced MIF values. This effect may be related to the fact that these surfaces induced more pronounced membrane alterations, as demonstrated by CLSM (Figs. 6 and 7A) and DiBAC$_4$(3) staining, suggesting that the affected cells were likely non-viable. Furthermore, previous studies (Hemelaar et al., 2018; Norouzi et al., 2022) have demonstrated that nanodiamonds are biocompatible and do not induce oxidative stress in mammalian or bacterial cells. Overall, the flow cytometry results suggest that the needles of bSi and bD surfaces change bacterial membrane permeability and compromise their metabolic activity.

3.4. Seawater exposure tests

To enhance the ecological relevance of this study, exposure tests using real seawater were conducted on materials commonly employed in marine environments (steel and Perspex), together with the control surface (Flat-Si) and the four active surfaces (bSi-OF, bSi-F, bD-H, and bD-F). The resulting biofilms were analyzed by OCT to quantify biofilm thickness (Fig. 8), contour coefficient, porosity, and the average size of non-connected pores (Fig. S5 in Supplementary Material). Representative 3D OCT reconstructions of the developed biofilms are also presented

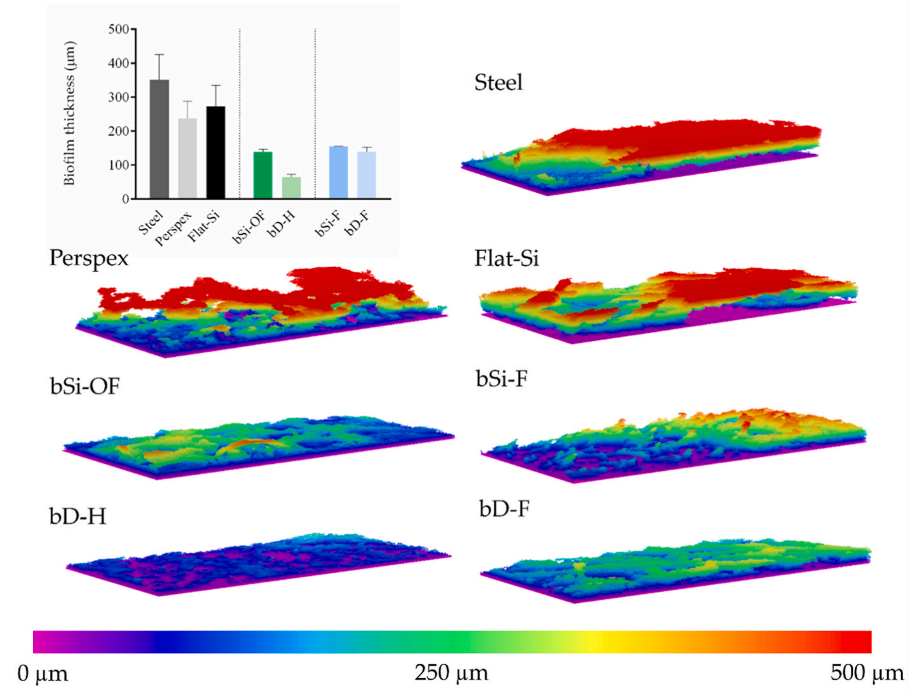

Fig. 8. Biofilm development after 4 weeks of exposure to real seawater on materials commonly employed in marine settings (steel and Perspex), the control surface (Flat-Si) and the four active surfaces (bSi-OF, bSi-F, bD-H, and bD-F). Biofilm thickness is shown in the graphical representation, with data presented as mean and SD from three replicates. Representative 3D OCT images of the biofilms are also shown; the colour scale indicates biofilm thickness (up to 500 μm). Thicker and more heterogeneous biofilms were observed on steel, Perspex, and Flat-Si, whereas thinner and smoother biofilms formed on the active surfaces.

in Fig. 8, and complementary SEM analysis was performed to assess biofilm distribution across the surfaces (Fig. 9).

Although biofilms developed over a shorter period (4 vs. 7 weeks), those formed *in vitro* under real seawater exposure and hydrodynamic conditions simulating marine environments were thicker and more heterogeneous than those formed by *C. marina* in VNSS medium under the same hydrodynamic conditions (Fig. 4). On Flat-Si surfaces, biofilm thickness reached 272 μm, compared to only 140 μm under VNSS, likely reflecting the enhanced colonization potential of natural seawater due to its greater species diversity. Moreover, biofilms on the control surfaces (steel, Perspex, and Flat-Si) were thicker than those on the four active surfaces (Fig. 8), with thickness reductions of 56-82% compared to steel. Biofouling increases hull roughness and hydrodynamic drag, which, in turn, reduces vessel speed and increases fuel consumption. Since fuel is the largest single operating cost for most vessels (accounting for up to 50% in bulk carriers), even small improvements in surface smoothness can yield substantial economic benefits. For instance, a 10 μm increase in average hull roughness has been estimated to raise fuel consumption by 0.3–1.0% (Champ, 2000). Consequently, the reduction in biofilm thickness observed on the active surfaces highlights their strong potential for application in marine antifouling strategies.

Representative 3D OCT images further highlighted architectural differences among the biofilms, with the control surfaces exhibiting streamers (up to 500 μm) and a highly heterogeneous structure, as reflected by higher contour coefficient values (Fig. S5A in Supplementary Material). Consistent with VNSS experiments (Fig. 3), Flat-Si exhibited the highest biofilm porosity and average non-connected pore volume (11% and 2458 μm^3, respectively; Fig. S5B, C in Supplementary Material), with steel and Perspex showing similar values. In contrast, porosity decreased to 2% on bD-H (Fig. S5B in Supplementary Material).

SEM analyses of biofilm formed with real seawater (Fig. 9) confirmed the OCT results. Steel, Perspex, and Flat-Si were fully covered by biofilm, while the bD-F surface showed uncolonized areas. Furthermore, the spiky structures of the active surfaces largely retained their integrity, most notably on bD-H and bD-F surfaces, where spikes visibly pierced through the biofilm.

To further assess the mechanical robustness and long-term durability of the nanostructured surfaces, bD-H and bD-F were subjected to additional field immersion tests (Section 6 of Supplementary Material). Both surfaces retained their structural integrity after prolonged exposure to a natural aquatic environment, confirming their stability and antifouling ability under realistic conditions.

4. Conclusions

This study presents a novel investigation into the efficacy of nanostructured black silicon (bSi) and black diamond (bD) surfaces, with either hydrogen or fluorine-terminated surfaces, in mitigating marine biofilm formation under defined hydrodynamic conditions over an extended duration of 49 days. While nanostructured surfaces like bSi have shown bactericidal effects in medical contexts, their marine application remains underexplored. Building on the known robustness and antimicrobial properties of diamond coatings, this work bridges the gap between static biomedical studies and real-world marine antifouling applications.

Contact angle measurements confirmed decreased wettability on all active surfaces, especially fluorine-terminated black diamond (bD-F), which showed the highest water repellency. SEM analysis revealed that the nanospike morphology of bSi and bD surfaces was maintained after 7 weeks, and these structures, particularly on bD-F, appeared to physically disrupt biofilms. Quantitative assays demonstrated that bSi-OF and bD-F significantly reduced biofilm thickness, porosity, and cell density. OCT data showed a marked reduction in biofilm thickness (up to 53%) and contour coefficient on bSi-OF and bD-F surfaces, suggesting more uniform and thinner biofilms. CLSM imaging corroborated these findings, indicating that the bD-F surface experienced the greatest reduction in

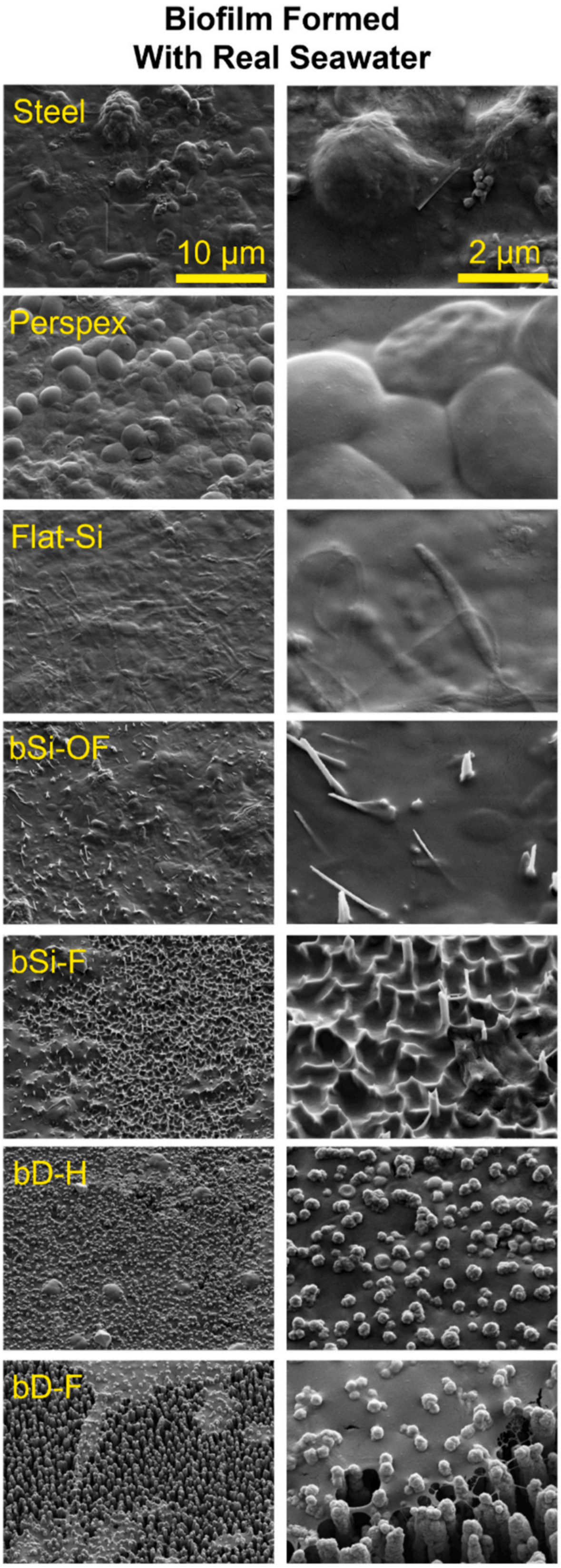

Fig. 9. SEM micrographs of the different surfaces after exposure to real seawater over 4 weeks. The left panels show the overall surface topography at 10,000 × magnification (scale bar = 10 μm), while the right panels provide higher-resolution details at 50,000 × magnification (scale bar = 2 μm). Biofilm covered control surfaces, while the spiky structures of active surfaces, especially bD-F, remained largely intact.

total biovolume compared to the Flat-Si control (75%). Moreover, it showed the lowest viability percentage (only 45%), with non-viable cells particularly concentrated at the biofilm-surface interface. This localized bactericidal effect may stem from the mechanical stress induced by the sharp, robust nanostructures, especially those reinforced with diamond coating. Flow cytometry further supported this observation, revealing alterations in bacterial membrane potential and metabolic activity in cells exposed to the bD surfaces, providing no evidence of oxidative stress-induced antimicrobial action.

The superior antifouling performance of bD-F compared to bD-H can be attributed to differences in surface chemistry and stability. Hydrogen-terminated surfaces, while moderately hydrophobic, are prone to partial oxidation in aqueous environments, leading to heterogeneity and higher surface energy that favor bacterial adhesion. In contrast, fluorine termination creates chemically robust, densely packed, and super-hydrophobic surfaces that shield underlying carbon atoms, reduce surface energy, and enhance repulsive forces. Together, these properties make bD-F effective for antifouling applications, highlighting fluorination as a key strategy for diamond-based antibacterial surfaces.

Additional tests with real seawater and field immersion assays confirmed that bD surfaces maintain their nanostructured integrity and effectively reduce biofouling under realistic marine conditions, demonstrating their robustness and practical applicability for long-term antifouling.

Building on these findings, longer-term solutions may focus on replicating the geometry, density, and mechanical robustness of the nanostructured bD spikes using materials that are less exotic and more cost-effective than black diamond, as coating the entire underside of a ship in bD would be expensive and impractical. As such, work is currently underway to develop a hard but flexible rubber material with similar nanostructured features, which would be much more compatible with marine applications. Such a flexible rubber layer could simply be attached to the surface needing protection, and either replaced with a new one when biofouling eventually occurred or cleaned *in situ* with water jets. If the duration required between cleaning could be increased by only a factor of two using methods such as these, the cost savings for marine applications would be significant.

CRediT authorship contribution statement

M.J. Romeu: Writing – original draft, Visualization, Methodology, Investigation, Formal analysis. **L.C. Gomes:** Writing – original draft, Visualization, Methodology, Investigation, Formal analysis. **R. Teixeira-Santos:** Writing – original draft, Visualization, Methodology, Investigation, Formal analysis. **G. Zulpukarova:** Writing – review & editing. **W. Woudstra:** Writing – review & editing, Visualization, Methodology, Investigation, Formal analysis. **J. Atema-Smit:** Writing – review & editing, Investigation, Formal analysis. **G. Geertsema-Doornbusch:** Formal analysis. **R. Schirhagl:** Writing – original draft, Supervision, Resources, Funding acquisition, Conceptualization. **P.W. May:** Writing – review & editing. **F.J. Mergulhão:** Writing – review & editing, Supervision, Resources, Funding acquisition, Conceptualization.

Declaration of competing interest

The authors declare the following financial interests/personal relationships which may be considered as potential competing interests: Romana Schirhagl reports a relationship with QTsense that includes: employment. If there are other authors, they declare that they have no known competing financial interests or personal relationships that could have appeared to influence the work reported in this paper.

Acknowledgements

Part of the work has been performed at the Giepmans lab, which is sponsored by ZonMW grant 91111.006 (ATLAS). This work was supported by national funds through FCT/MECI: LEPABE, UID/00511/2025 (https://doi.org/10.54499/UID/00511/2025) and UID/PRR/00511/2025 (https://doi.org/10.54499/UID/PRR/00511/2025), ALiCE, LA/P/0045/2020 (https://doi.org/10.54499/LA/P/0045/2020), and project NanoBioMitig (DOI: 10.54499/2022.06149.PTDC). M.J.R. acknowledges the receipt of a junior researcher fellowship from the project 2022.05314.PTDC (BacAllFree). R.T.-S. thanks FCT for the financial support of her work contract through the Scientific Employment Stimulus — Individual Call — 2023.07999.CEECIND/CP2834/CT0014 (DOI: 10.54499/2023.07999.CEECIND/CP2834/CT0014). GZ thanks the funding scheme of the Government of the Republic of Kazakhstan under the Bolashak International program.

Appendix A. Supplementary data

Supplementary data to this article can be found online at https://doi.org/10.1016/j.envres.2026.124321.

Data availability

Data will be made available on request.

References

Alexandrou, A., 2001. Principles of Fluid Mechanics. Prentice Hall, Upper Saddle River, N.J.

Alves, P., Gomes, L.C., Rodríguez-Emmenegger, C., Mergulhão, F.J., 2020. Efficacy of A Poly(MeOEGMA) brush on the prevention of *Escherichia coli* biofilm formation and susceptibility. Antibiotics 9, 216. https://doi.org/10.3390/antibiotics9050216.

Arahal, D.R., Castillo, A.M., Ludwig, W., Schleifer, K.H., Ventosa, A., 2002. Proposal of *Cobetia marina* gen. nov., comb. nov., within the family *Halomonadaceae*, to include the species *Halomonas marina*. Syst. Appl. Microbiol. 25, 207–211. https://doi.org/10.1078/0723-2020-00113.

Bakker, D.P., Plaats, A. Van Der, Verkerke, G.J., Busscher, H.J., Mei, H.C. Van Der, 2003. Comparison of velocity profiles for different flow chamber designs used in studies of microbial adhesion to surfaces. Appl. Environ. Microbiol. 69, 6280–6287. https://doi.org/10.1128/AEM.69.10.6280.

Bas, S., Kramer, M., Stopar, D., 2017. Biofilm surface density determines biocide effectiveness. Front. Microbiol. 8, 1–9. https://doi.org/10.3389/fmicb.2017.02443.

Bhadra, C.M., Werner, M., Baulin, V.A., Truong, V.K., Kobaisi, M. Al, Nguyen, S.H., Balcytis, A., Juodkazis, S., Wang, J.Y., Mainwaring, D.E., Crawford, R.J., Ivanova, E. P., 2018. Subtle variations in surface properties of black silicon surfaces influence the degree of bactericidal efficiency. Nano-Micro Lett. 10, 36. https://doi.org/10.1007/s40820-017-0186-9.

Blain, S., Guillou, J., Tréguer, P.J., Woerther, P., Delauney, L., Follenfant, E., Gontier, O., Hamon, M., Leilde, B., Mer, D., Cnrs, U.M.R., Nicolas, P., Mer, D., Cnrs, F.R., Copernic, P.N., 2004. High frequency monitoring of the coastal marine environment using the MAREL buoy. J. Environ. Monit. 6, 569–575. https://doi.org/10.1016/S0005-2728(89)80347-0.

Carvalho, C.C.C.R., 2018. Marine biofilms: a successful microbial strategy with economic implications. Front. Mar. Sci. 5, 1–11. https://doi.org/10.3389/fmars.2018.00126.

Carvalho, F.M., Gomes, L.C., Teixeira-Santos, R., Carapeto, A.P., Mergulhão, F.J., Almada, S., Silva, E.R., Alves, L.G., 2025. New cyclam-based Fe(III) complexes coatings targeting *Cobetia marina* biofilms. Molecules 30, 917. https://doi.org/10.3390/molecules30040917.

Champ, M.A., 2000. A review of organotin regulatory strategies, pending actions, related costs and benefits. Sci. Total Environ. 258, 21–71. https://doi.org/10.1016/S0048-9697(00)00506-4.

da Silva Domingues, J.F., van der Mei, H.C., Busscher, H.J., van Kooten, T.G., 2013. Phagocytosis of bacteria adhering to a biomaterial surface in a surface thermodynamic perspective. PLoS One 8, e70046. https://doi.org/10.1371/journal.pone.0070046.

Ding, X., Duan, S., Ding, X., Liu, R., Xu, F.-J., 2018. Versatile antibacterial materials: an emerging arsenal for combatting bacterial pathogens. Adv. Funct. Mater. 28, 1802140. https://doi.org/10.1002/adfm.201802140.

Doiron, K., Beaulieu, L., St-Louis, R., Lemarchand, K., 2018. Reduction of bacterial biofilm formation using marine natural antimicrobial peptides. Colloids Surf. B Biointerfaces 167, 524–530. https://doi.org/10.1016/j.colsurfb.2018.04.051.

Dunseath, O., Smith, E.J.W., Al-Jeda, T., Smith, J.A., King, S., May, P.W., Nobbs, A.H., Hazell, G., Welch, C.C., Su, B., 2019. Studies of black diamond as an antibacterial surface for gram negative bacteria: the interplay between chemical and mechanical bactericidal activity. Sci. Rep. 9, 8815. https://doi.org/10.1038/s41598-019-45280-2.

Faria, S., Teixeira-Santos, R., Romeu, M.J., Morais, J., Jong, E. de, Sjollema, J., Vasconcelos, V., Mergulhão, F.J., 2021. Unveiling the antifouling performance of different marine surfaces and their effect on the development and structure of cyanobacterial biofilms. Microorganisms 9, 1102. https://doi.org/10.3390/microorganisms9051102.

Flemming, H., Wingender, J., 2010. The biofilm matrix. Nat. Rev. Microbiol. 8, 623–633. https://doi.org/10.1038/nrmicro2415.

Ghattavi, S., Homaei, A., 2024. Synthesis and characterization of ZnO-SiO2 hybrid nanoparticles as an effective inhibitor for marine biofilm and biofouling. J. Mol. Liq. 396, 123974. https://doi.org/10.1016/j.molliq.2024.123974.

Ghattavi, S., Homaei, A., Kamrani, E., 2025. Innovative CuO-melanin hybrid nanoparticles and polytetrafluoroethylene for enhanced antifouling coatings. Colloids Surf. B Biointerfaces 246, 114387. https://doi.org/10.1016/j.colsurfb.2024.114387.

Ghattavi, S., Homaei, A., Kamrani, E., Saberi, D., Daliri, M., 2023. Fabrication of antifouling coating based on chitosan-melanin hybrid nanoparticles as sustainable and antimicrobial surface. Prog. Org. Coating 174, 107327. https://doi.org/10.1016/j.porgcoat.2022.107327.

Ghattavi, S., Kamrani, E., Homaei, A., 2024. Green synthesis of ZnO-chitosan nanoparticles and vinyl resin with effective antifouling properties. Prog. Org. Coating 194, 108615. https://doi.org/10.1016/j.porgcoat.2024.108615.

Gomes, M., Gomes, L.C., Teixeira-Santos, R., Pereira, M.F.R., Soares, O.S.G.P., Mergulhão, F.J., 2022. Carbon nanotube-based surfaces: effect on the inhibition of single- and dual-species biofilms of *Escherichia coli* and *Enterococcus faecalis*. Results Surf. Interfaces 9, 100090. https://doi.org/10.1016/j.rsurfi.2022.100090.

Gorth, D.J., Puckett, S., Ercan, B., Webster, T.J., Rahaman, M., Bal, B.S., 2012. Decreased bacteria activity on Si_3N_4 surfaces compared with PEEK or titanium. Int. J. Nanomed. 7, 4829–4840. https://doi.org/10.2147/IJN.S35190.

Harper, P., Hallett, S., Fleming, A., Dawson, M., 2016. Advanced fibre-reinforced composites for marine renewable energy devices. In: Graham-Jones, J., Summerscales, J. (Eds.), Woodhead Publishing Series in Composites Science and Engineering. Woodhead Publishing, pp. 217–232.. https://doi.org/10.1016/B978-1-78242-250-1.00009-0. Marine Applications of Advanced Fibre-Reinforced Composites.

Hazell, G., May, P.W., Taylor, P., Nobbs, A.H., Welch, C.C., Su, B., 2018. Studies of Black silicon and black diamond as materials for antibacterial surfaces. Biomater. Sci. 6, 1424–1432. https://doi.org/10.1039/C8BM00107C.

Hemelaar, S.R., Saspaanithy, B., L'Hommelet, S.R.M., Perona Martinez, F.P., van der Laan, K.J., Schirhagl, R., 2018. The response of HeLa cells to fluorescent NanoDiamond uptake. Sensors 18, 355. https://doi.org/10.3390/s18020355.

Hermansson, M., 1999. The DLVO theory in microbial adhesion. Colloids Surf. B Biointerfaces 14, 105–119. https://doi.org/10.1016/S0927-7765(99)00029-6.

Herzberg, M., Berglin, M., Eliahu, S., Bodin, L., Agrenius, K., Zlotkin, A., Svenson, J., 2021. Efficient prevention of marine biofilm formation employing a surface-grafted Repellent marine peptide. ACS Appl. Bio Mater. 4, 3360–3373. https://doi.org/10.1021/acsabm.0c01672.

Heydorn, A., Nielsen, A.T., Hentzer, M., Sternberg, C., Givskov, M., Ersboll, B.K., Molin, S., 2000. Quantification of biofilm structures by the novel computer program COMSTAT. Microbiology 146, 2395–2407. https://doi.org/10.1099/00221287-146-10-2395.

Ivanova, E.P., Hasan, J., Webb, H.K., Gervinskas, G., Juodkazis, S., Truong, V.K., Wu, A. H.F., Lamb, R.N., Baulin, V.A., Watson, G.S., Watson, J.A., Mainwaring, D.E., Crawford, R.J., 2013. Bactericidal activity of black silicon. Nat. Commun. 4, 2838. https://doi.org/10.1038/ncomms3838.

Jenkins, J., Ishak, M.I., Eales, M., Gholinia, A., Kulkarni, S., Keller, T.F., May, P.W., Nobbs, A.H., Su, B., 2021. Resolving physical interactions between bacteria and nanotopographies with focused ion beam scanning electron microscopy. iScience 24, 102818. https://doi.org/10.1016/j.isci.2021.102818.

Karyani, T.Z., Ghattavi, S., Homaei, A., 2023. Application of enzymes for targeted removal of biofilm and fouling from fouling-release surfaces in marine environments: a review. Int. J. Biol. Macromol. 253, 127269. https://doi.org/10.1016/j.ijbiomac.2023.127269.

King, R.K., Flick, G.J., Pierson, M.D., Smith, S. a, Boardman, G.D., Coale, C.W., 2004. Identification of bacterial pathogens in biofilms of recirculating aquaculture systems. J. Aquat. Food Prod. Technol. 13, 125–133. https://doi.org/10.1300/J030v13n01.

King, R.K., Flick, G.J., Smith, S.A., Pierson, M.D., Boardman, G.D., Coale, C.W., 2006. Comparison of bacterial presence in biofilms on different materials commonly found in recirculating aquaculture systems. J. Appl. Aquacult. 18, 79–88. https://doi.org/10.1300/J028v18n01.

Lacoursière-Roussel, A., Bock, D.G., Cristescu, M.E., Guichard, F., McKindsey, C.W., 2016. Effect of shipping traffic on biofouling invasion success at population and community levels. Biol. Invasions 18, 3681–3695. https://doi.org/10.1007/s10530-016-1258-3.

Lelchat, F., Cérantola, S., Brandily, C., Colliec-Jouault, S., Baudoux, A.-C., Ojima, T., Boisset, C., 2015. The marine bacteria *Cobetia marina* DSMZ 4741 synthesizes an unexpected K-antigen-like exopolysaccharide. Carbohydr. Polym. 124, 347–356. https://doi.org/10.1016/j.carbpol.2015.02.038.

Lima, M., Gomes, L.C., Teixeira-santos, R., Romeu, M.J., Valcárcel, J., Vázquez, J.A., Cerqueira, M.A., Pastrana, L., Bourbon, A.I., Jong, E.D.D., Sjollema, J., Mergulhão, F. J., 2022. Assessment of the antibiofilm performance of chitosan-based surfaces in marine environments. Int. J. Mol. Sci. 23, 14647. https://doi.org/10.3390/ijms232314647.

Linklater, D.P., Nguyen, H.K.D., Bhadra, C.M., Juodkazis, S., Ivanova, E.P., 2017. Influence of nanoscale topology on bactericidal efficiency of black silicon surfaces. Nanotechnology 28, 245301. https://doi.org/10.1088/1361-6528/aa700e.

López Cascales, J.J., Zenak, S., García de la Torre, J., Lezama, O.G., Garro, A., Enriz, R. D., 2018. Small cationic peptides: influence of charge on their antimicrobial activity. ACS Omega 3, 5390–5398. https://doi.org/10.1021/acsomega.8b00293.

Luan, Y., Liu, S., Pihl, M., van der Mei, H.C., Liu, J., Hizal, F., Choi, C.-H., Chen, H., Ren, Y., Busscher, H.J., 2018. Bacterial interactions with nanostructured surfaces. Curr. Opin. Colloid Interface Sci. 38, 170–189. https://doi.org/10.1016/j.cocis.2018.10.007.

Mansour, A., Liu, D., 2008. The Principles of Naval Architecture Series: Strength of Ships and Ocean Structures. The Society of Naval Architects and Marine Engineers, Jersey City, NJ.

Mårdén, P., Tunlid, A., Malmcrona-Friberg, K., Odham, G., Kjelleberg, S., 1985. Physiological and morphological changes during short term starvation of marine bacterial islates. Arch. Microbiol. 142, 326–332. https://doi.org/10.1007/BF00491898.

May, P.W., 2000. Diamond thin films: a 21st-century material. Philos. Trans. R. Soc. London. Ser. A Math. Phys. Eng. Sci. 358, 473–495. https://doi.org/10.1098/rsta.2000.0542.

May, P.W., Clegg, M., Silva, T.A., Zanin, H., Fatibello-Filho, O., Celorrio, V., Fermin, D.J., Welch, C.C., Hazell, G., Fisher, L., Nobbs, A., Su, B., 2016. Diamond-coated "black silicon" as a promising material for high-surface-area electrochemical electrodes and antibacterial surfaces. J. Mater. Chem. B 4, 5737–5746. https://doi.org/10.1039/c6tb01774f.

Mieszkin, S., Callow, M.E., Callow, J.A., 2013. Interactions between microbial biofilms and marine fouling algae: a mini review. Biofouling 29, 1097–1113. https://doi.org/10.1080/08927014.2013.828712.

Mitik-Dineva, N., Wang, J., Truong, V.K., Stoddart, P., Malherbe, F., Crawford, R.J., Ivanova, E.P., 2009. *Escherichia coli*, *Pseudomonas aeruginosa*, and *Staphylococcus aureus* attachment patterns on glass surfaces with nanoscale roughness. Curr. Microbiol. 58, 268–273. https://doi.org/10.1007/s00284-008-9320-8.

Neves, A.R., Gomes, L.C., Faria, S.I., Sousa, J., Ruivo, R., Páscoa, I., Pinto, M., Sousa, E., Santos, M.M., Silva, E.R., Correia-da-Silva, M., Mergulhão, F., 2022. Antifouling marine coatings with a potentially safer and sustainable synthetic polyphenolic derivative. Mar. Drugs. 30, 917. https://doi.org/10.3390/md20080507.

Norouzi, N., Nusantara, A.C., Ong, Y., Hamoh, T., Nie, L., Morita, A., Zhang, Y., Mzyk, A., Schirhagl, R., 2022. Relaxometry for detecting free radical generation during Bacteria's response to antibiotics. Carbon N. Y. 199, 444–452. https://doi.org/10.1016/j.carbon.2022.08.025.

Norouzi, N., Ong, Y., Damle, V.G., Habibi Najafi, M.B., Schirhagl, R., 2020. Effect of medium and aggregation on antibacterial activity of nanodiamonds. Mater. Sci. Eng., C 112, 110930. https://doi.org/10.1016/j.msec.2020.110930.

Norouzi, N., Woudstra, W., Smith, E.J.W., Zulpukarova, G., Yao, K., Damle, V.G., Schirhagl, R., May, P.W., Kamp, T., 2023. Antimicrobial studies of black silicon and black diamond using gram-positive bacteria. Adv. Eng. Mater. 25, 2301031. https://doi.org/10.1002/adem.202301031.

Oh, J.K., Yegin, Y., Yang, F., Zhang, M., Li, J., Huang, S., Verkhoturov, S.V., Schweikert, E.A., Perez-Lewis, K., Scholar, E.A., Taylor, T.M., Castillo, A., Cisneros-Zevallos, L., Min, Y., Akbulut, M., 2018. The influence of surface chemistry on the kinetics and thermodynamics of bacterial adhesion. Sci. Rep. 8, 17247. https://doi.org/10.1038/s41598-018-35343-1.

Ong, S.Y., van Harmelen, R.J.J., Norouzi, N., Offens, F., Venema, I.M., Habibi Najafi, M. B., Schirhagl, R., 2018. Interaction of nanodiamonds with bacteria. Nanoscale 10, 17117–17124. https://doi.org/10.1039/C8NR05183F.

Otsu, N., 1979. A threshold selection method from gray-level histograms. IEEE Trans. Syst. Man Cybern. 9, 62–66. https://doi.org/10.1109/TSMC.1979.4310076.

Park, J., Jang, G.H., Jung, Y.W., Seo, H., Han, H.-S., Lee, J., Seo, Y., Jeon, H., Ok, M.-R., Cha, P.-R., Seok, H.-K., Lee, K.H., Kim, Y.-C., 2020. Tailoring H(2)O(2) generation kinetics with magnesium alloys for efficient disinfection on titanium surface. Sci. Rep. 10, 6536. https://doi.org/10.1038/s41598-020-63007-6.

Paxton, W.F., Rozsa, J.L., Brooks, M.M., Running, M.P., Schultz, D.J., Jasinski, J.B., Jung, H.J., Akram, M.Z., 2021. A scalable approach to topographically mediated antimicrobial surfaces based on diamond. J. Nanobiotechnol. 19, 458. https://doi.org/10.1186/s12951-021-01218-3.

Peterson, B.W., He, Y., Ren, Y., Zerdoum, A., Libera, M.R., Sharma, P.K., van Winkelhoff, A.J., Neut, D., Stoodley, P., van der Mei, H.C., Busscher, H.J., 2015. Viscoelasticity of biofilms and their recalcitrance to mechanical and chemical challenges. FEMS Microbiol. Rev. 39, 234–245. https://doi.org/10.1093/femsre/fuu008.

Peterson, B.W., van der Mei, H.C., Sjollema, J., Busscher, H.J., Sharma, P.K., Chapman, M., Hultgren, S.J., 2021. A distinguishable role of eDNA in the viscoelastic relaxation of biofilms. MBio 4, e00497-13. https://doi.org/10.1128/mBio.00497-13.

Qian, P.-Y., Cheng, A., Wang, R., Zhang, R., 2022. Marine biofilms: diversity, interactions and biofouling. Nat. Rev. Microbiol. 20, 671–684. https://doi.org/10.1038/s41579-022-00744-7.

Romeu, M.J., Alves, P., Morais, J., Miranda, J.M., de Jong, E.D., Sjollema, J., Ramos, V., Vasconcelos, V., Mergulhão, F.J.M., 2019. Biofilm formation behaviour of marine filamentous cyanobacterial strains in controlled hydrodynamic conditions. Environ. Microbiol. 21, 4411–4424. https://doi.org/10.1111/1462-2920.14807.

Romeu, M.J., Lima, M., Gomes, L.C., Jong, E.D. De, Morais, J., Vasconcelos, V., Pereira, M.F.R., Soares, S.G.P., Sjollema, J., Mergulhão, F.J., 2022. The use of 3D optical coherence tomography to analyze the architecture of cyanobacterial biofilms formed on a carbon nanotube composite. Polymers 14, 4410. https://doi.org/10.3390/polym14204410.

Romeu, M.J., Miranda, J.M., de Jong, E.D., Morais, J., Vasconcelos, V., Sjollema, J., Mergulhão, F.J., 2024. Understanding the flow behavior around marine biofilms. Biofilm 7, 100204. https://doi.org/10.1016/j.bioflm.2024.100204.

Roy, G.J., 1994. Notes on Instrumentation and Control (Marine Engineering). Newnes, Oxford, Boston.

Salta, M., Wharton, J.A., Blache, Y., Stokes, K.R., Briand, J.F., 2013. Marine biofilms on artificial surfaces: structure and dynamics. Environ. Microbiol. 15, 2879–2893. https://doi.org/10.1111/1462-2920.12186.

Sen, F.G., Qi, Y., Alpas, A.T., 2009. Surface stability and electronic structure of hydrogen- and fluorine-terminated diamond surfaces: a first principles investigation. J. Mater. Res. 24, 2461–2470. https://doi.org/10.1557/jmr.2009.0309.

Silva, E.R., Tulcidas, A.V., Ferreira, O., Bayón, R., Igartua, A., Mendoza, G., Mergulhão, F.J.M., Faria, S.I., Gomes, L.C., Carvalho, S., Bordado, J.C.M., 2021. Assessment of the environmental compatibility and antifouling performance of an innovative biocidal and foul-release multifunctional marine coating. Environ. Res. 198, 111219. https://doi.org/10.1016/j.envres.2021.111219.

Sousa-Cardoso, F., Teixeira-Santos, R., Campos, A.F., Lima, M., Gomes, L.C., Soares, O.S. G.P., Mergulhão, F.J., 2023. Graphene-based coating to mitigate biofilm development in marine environments. Nanomaterials 13, 381. https://doi.org/10.3390/nano13030381.

Tang, R.J., Cooney, J.J., 1998. Effects of marine paints on microbial biofilm development on three materials. J. Ind. Microbiol. Biotechnol. 20, 275–280. https://doi.org/10.1038/sj.jim.2900523.

Taylor, D.A., 1996. Introduction to Marine Engineering. Butterworth-Heinemann, United Kingdom. https://doi.org/10.1007/s11103-011-9767-z.Plastid.

van der Mei, H.C., White, D.J., Kamminga-Rasker, H.J., Knight, J., Baig, A.A., Smit, J., Busscher, H.J., 2002. Influence of dentifrices and dietary components in saliva on wettability of pellicle-coated enamel in vitro and in vivo. Eur. J. Oral Sci. 110, 434–438. https://doi.org/10.1034/j.1600-0722.2002.21341.x.

Xie, M., Zhao, W., Wu, Y., 2021. Preventing algae biofilm formation via designing long-term oil storage surfaces for excellent antifouling performance. Appl. Surf. Sci. 554, 149612. https://doi.org/10.1016/j.apsusc.2021.149612.

Yang, Y., Cai, Z., Huang, Z., Tang, X., Zhang, X., 2018. Antimicrobial cationic polymers: from structural design to functional control. Polym. J. 50, 33–44. https://doi.org/10.1038/pj.2017.72.

Yonezawa, K., Kawaguchi, M., Kaneuji, A., Ichiseki, T., Iinuma, Y., Kawamura, K., Shintani, K., Oda, S., Taki, M., Kawahara, N., 2020. Evaluation of antibacterial and cytotoxic properties of a fluorinated diamond-like carbon coating for the development of antibacterial medical implants. Antibiotic 9, 495. https://doi.org/10.3390/antibiotics9080495.

Zhang, J., Huang, J., Say, C., Dorit, R.L., Queeney, K.T., 2018. Deconvoluting the effects of surface chemistry and nanoscale topography: pseudomonas aeruginosa biofilm nucleation on Si-based substrates. J. Colloid Interface Sci. 519, 203–213. https://doi.org/10.1016/j.jcis.2018.02.068.

Zheng, S., Bawazir, M., Dhall, A., Kim, H.E., He, L., Heo, J., Hwang, G., 2021. Implication of surface properties, bacterial motility, and hydrodynamic conditions on bacterial surface sensing and their initial adhesion. Front. Bioeng. Biotechnol. 9, 1–22. https://doi.org/10.3389/fbioe.2021.643722.

Ziębowicz, A., Sambok-Kiełbowicz, A., Walke, W., Mzyk, A., Kosiel, K., Kubacki, J., Bączkowski, B., Pawlyta, M., Ziębowicz, B., 2021. Evaluation of bacterial adhesion to the ZrO2 atomic layer deposited on the surface of cobalt-chromium dental alloy produced by DMLS method. Materials 14, 1079. https://doi.org/10.3390/ma14051079.